

Thesis Title

A subtitle of your thesis

Author name



Thesis submitted for the degree of
Master in Master's Program Name <change at
main.tex>
60 credits

Department Name <change at main.tex>
Faculty name <change in duoforside.tex>

UNIVERSITY OF OSLO

Spring 2022

Thesis Title

A subtitle of your thesis

Author name

© 2022 Author name

Thesis Title

<http://www.duo.uio.no/>

Printed: Reprosentralen, University of Oslo

Abstract

Contents

1	Introduction	1
I Theory		3
2	High-Entropy alloys	4
2.1	Fundamentals	4
2.2	Core effects and properties	7
3	Modeling of random alloys	9
3.1	The Special Quasi-random Structure model	9
3.1.1	Mathematical description	10
3.1.2	Applications to high-entropy alloys	12
4	Density Functional Theory	16
4.1	Review of Quantum Mechanics	17
4.1.1	The Shrodinger equation	17
4.1.2	Approximations to the many-body Shrodinger equation	18
4.2	Kohn-Sham density functional theory	20
4.2.1	Density functional theory	20
4.2.2	The Kohn-Sham Equation	21
4.3	Limitations of DFT - Insert refs	22
II Methodology and Implementation		24
5	Practical application of DFT	25
5.1	The Exchange-Correlation functional	25
5.1.1	Local density approximation	25
5.1.2	Generalized gradient approximation	26
5.1.3	Meta-GGA	26
5.1.4	Hybrid functionals	27
5.1.5	Outlook	27
5.2	Fundamental aspects of practical DFT calculations	28
5.3	Self-consistent field calculation	30

6 Computational details	32
6.1 Vienna Ab initio Simulation Package	32
6.2 Generation of SQS	34
6.3 Utility scripts	35
III Results and Discussion	37
7 The results of (CrFeMnNi)Si₂ in the β–FeSi₂ structure	39
7.1 Eqvimolar SQSs	39
7.1.1 Introduction	39
7.1.2 The band gap	40
7.1.3 Local and Projected density of states	42
7.1.4 Meta-GGA and hybrid functional	46
7.1.5 Probability distribution functions and charge density	50
7.2 Permutations of the Cr ₄ Fe ₄ Mn ₄ Ni ₄ Si ₃₂ high-entropy silicide	52
8 Changing the elements	59
9 Overview and Outlook	63
9.1 Cr ₄ Fe ₄ Mn ₄ Ni ₄ Si ₃₂ in different crystal structures	63
9.2 Overview	65
IV Conclusion	66
A Compositions	68
A.1 Projected density of states	68
A.2 Probability distribution functions	71
B PDFs	73
C Charge density	74

List of Figures

2.1	Formation of HEA based on δ and N . Figures adopted from [2]	6
2.2	A schematic illustration of lattice distortion in high-entropy alloys. Figure from [5]	8
3.1	PDFs of (a) 20 and (b) 250 atom SQS models of CrFeMnNi [10]	13
3.2	Density of states with SQS and MC/MD of FCC CoCrFeNi, figure from [10]	14
3.3	Probability distribution functions with SQS and MC/MD of HCP CoOsReRu [10]	14
4.1	Number of DFT studies per year from 1980 to 2021 [16].	16
5.1	Calculated to experimental band gap measurements of Becke-Johnsoon, modified Becke-Johnson and SCAN functionals [36]	27
5.2	Self consistent iteration of a DFT calculation. Figure adopted from lecture notes fys-mena4111 cite	31
6.1	48 atom SQS based on eqvimolar distribution of Cr, Fe, Mn and Ni in and $FeSi_2$ cell.	36
7.1	Density of states SQS D CFMN (fesi2) from PBE calculation .	41
7.2	Density of states SQS B CFMN (fesi2) from PBE calculation .	42
7.3	Local density of states of Si (SQS D)	43
7.4	Local density of states of TMs (SQS D), (a) Cr, (b) Mn, (c) Fe, (d) Ni	43
7.5	Projected density of states SQS D CFMN (fesi2) from PBE calculation	44
7.6	Projected density of states of SQS D and B around E_F	44
7.7	Density of states of SQS C with 2501 points vs 20000 points in the density of states.	45
7.8	Density of states of SQS E illustrating the different band gap from calculations with (a) PBE and (b) SCAN functional	47
7.9	Total density of states of SQS (a) B and (b) E from calculations with HSE06	48
7.10	Probability distribution function of SQS D (top) and B (bottom)	51
7.11	Charge density of SQS D and B from PBE calculations. Illustrated by VESTA	52

7.12	Projected density of states of (a) $\text{Cr}_3\text{Fe}_3\text{Mn}_7\text{Ni}_3\text{Si}_{32}$ (SQS B), (b) $\text{Cr}_5\text{Fe}_5\text{Mn}_3\text{Ni}_3\text{Si}_{32}$ (SQS C), (c) $\text{Cr}_5\text{Fe}_3\text{Mn}_5\text{Ni}_3\text{Si}_{32}$ (SQS A), (d) $\text{Cr}_3\text{Fe}_5\text{Mn}_5\text{Ni}_3\text{Si}_{32}$ (SQS D)	55
7.13	Density of states around E_F of SQS D and E $\text{Cr}_5\text{Fe}_5\text{Mn}_3\text{Ni}_3\text{Si}_{32}$	56
7.14	Projected density of states of $\text{Cr}_3\text{Fe}_3\text{Mn}_3\text{Ni}_7\text{Si}_{32}$ around E_F	56
7.15	Probability distribution functions to $\text{Cr}_3\text{Fe}_5\text{Mn}_5\text{Ni}_3\text{Si}_{32}$ SQS D, Maybe make larger	57
8.1	Probability distribution function of $\text{Co}_4\text{Fe}_4\text{Mn}_4\text{Ni}_4\text{Si}_{32}$ (top) and $\text{Cr}_4\text{Fe}_4\text{M}_4\text{Ti}_4\text{Si}_{32}$ (bottom)	60
8.2	Density of states of A: CrFeCoNiSi_2 , B: CrFeTiNiSi_2 , C: CoFeMnNiSi ₂ , D: CrFeMnCoSi ₂ , E: CrFeMnTiSi ₂ . Calcula- tions performed with PBE GGA.	61
A.1	chCr4Fe4Co4Ni4Si32	68
A.2	chCo4Fe4Mn4Ni4Si32	69
A.3	chCr4Fe4Mn4Co4Si32	69
A.4	chCr4Fe4Ti4Ni4Si32	70
A.5	chCr4Fe4Mn4Ti4Si32	70
A.6	Probability distribution functions of top: $\text{Co}_4\text{Fe}_4\text{Mn}_4\text{Ni}_4\text{Si}_{32}$ (SQS D), middle: $\text{Cr}_4\text{Fe}_4\text{Co}_4\text{Ni}_4\text{Si}_{32}$ (SQS B), bottom: $\text{Cr}_4\text{Fe}_4\text{Mn}_4\text{Co}_4\text{Si}_{32}$ (SQS B)	71
A.7	Probability distribution function of top: $\text{Cr}_4\text{Fe}_4\text{Mn}_4\text{Ti}_4\text{Si}_{32}$ (SQS B), bottom: $\text{Cr}_4\text{Fe}_4\text{Ti}_4\text{Ni}_4\text{Si}_{32}$ (SQS B))	72

List of Tables

7.1	Total energy per atom, final magnetic moment, band gap (GGA) and formation enthalpy of $Cr_4Fe_4Mn_4Ni_4Si_{32}$ SQSs based on $FeSi_2$	40
7.2	Band gap transition of CFMN (fesi2) SQSs with PBE functional	41
7.3	Band gap (eV) with PBE in spin up and spin down channels of CFMN (fesi2) SQSs	42
7.4	Band gap of CFMN ($FeSi_2$) SQSs with GGA (PBE), meta-GGA (SCAN) and hybrid-functionals (HSE06).	46
7.5	Mean and standard deviation of the total energy and magnetic moment per atom, plus enthalpy of formation of the listed mean energies ($FeSi_2$).	53
7.6	Total and spin dependent band gap of 4 permutations of CFMN (fesi2) with PBE GGA calculation. The structures that are excluded from this list either failed in calculations, or does not show any band gap.<	54
8.1	Summary of the total energy, enthalpy of formation and magnetization of several compositionally different SQS high-entropy alloys based on the β - $FeSi_2$ unit cell.	59

Preface

Chapter 1

Introduction

some introduction on the importance of discovering new materials and alloying.

Need something on thermoelectricity related to both the band gap and high-entropy alloys.

High-entropy alloys is a novel class of materials based on alloying multiple components, as opposed to the more traditional binary alloys. This results in an unprecedented opportunity for discovery of new materials with a superior degree of tuning for specific properties and applications. Recent research on high-entropy alloys have resulted in materials with exceedingly strong mechanical properties such as strength, corrosion and temperature resistance, etc **find references**. Meanwhile, the functional properties of high-entropy alloys is vastly unexplored. In this study, we attempt to broaden the knowledge of this field, the precise formulation of this thesis would be an exploration on the possibilities of semiconducting high-entropy alloys.

A key motivation of this thesis is the ability to perform such a broad study of complex materials in light of the advances in material informatics and computational methods. In this project, we will employ Ab initio methods backed by density functional theory on top-of the line supercomputers and software. 20 years ago, at the breaking point of these methods, this study would have been significantly narrower and less detailed firstly, but secondly would have totaled ... amount of CPU hours to complete (**Calculate this number**). In the addition to the development in computational power, is also the progress of modeling materials, specifically we will apply a method called Special Quasi-random Structures (SQS) to model high-entropy alloys or generally computationally complex structures. Together with the open landscape of high-entropy alloys described above, these factors produce a relevant study in the direction of applying modern computational methods to progress the research of a novel material class and point to promising directions for future research.

In specifics, this thesis revolve around the electrical properties of high-entropy alloys, mainly the band gap as this is the key indicator for a semiconducting material and it's applicability. Semiconductors are the building blocks in many different applications in today's world, ranging

from optical and electrical devices, to renewable energy sources such as solar and thermoelectricity. Given the economic and sustainable factors concerning silicon, in addition to its role in relevant applications such as microelectronics and solar power. Silicon emerges as a natural selection to build our alloys around. Furthermore, the development and research on both high entropy alloys and metal silicides have been heavily centered around 3d transition metals. Keeping in line with the economic and environmental factors, we will continue this direction by focusing on high entropy stabilized sustainable and economic 3d metal silicides **Not happy with this writing**. Throughout the study we will analyze a great number of permutations of 3d silicides, from different initial metal silicides such as $CrSi_2$, $FeSi_2$, $MnSi_{1.75}$, Fe_2Si , each with distinct properties relating to the band gap, crystal structure and metal to silicon ratio. In addition, the permutations include numerous metal distributions and elements within the 3d-group of metals. Examples are Co, Cr, Fe, Mn, and Ni.

Given a background in high-entropy alloys, one could ask if this study is truly sensible. In the later sections we will cover the details of this field, and it quickly become clear that the materials investigated in this study does not fall under the precise definition of high-entropy alloys, nor do we intend to explore the properties and factors relating to high-entropy stabilized alloys such as the configurational entropy, phase stability and finite temperature studies. However this study is motivated from the discovery of these materials and promising properties, and venture into a more hypothetical space of materials, enabled by the computational methods available to study the potential properties of such materials. On the other hand, very recent studies **Mari, and other HEA silicide study** have experimentally synthesized high-entropy disilicides, thus in some way justifying the direction of this project.

We begin this project by reviewing key concepts of solid-state physics for readers lacking a background in materials science, and an introduction to the base 3d silicides of the experimental work. Later follows a theoretic walk-through of the relevant concepts of this thesis, these topics include high-entropy alloys, special quasi-random structures, and density functional theory. Next we shine light on the implementation of DFT in this project, and other computational details required to reproduce the results in this thesis, such as the use of the Vienna Ab Initio Simulation Package (VASP) and implementation of SQS. Finally we present the results of our study, these include the band gap and electronic properties of various structures and the success and challenges of the computational methods applied throughout the study.

Part I

Theory

Chapter 2

High-Entropy alloys

To begin this project, we give a brief description of high-entropy alloys (HEA). We introduce the basics and definitions, as well some more advanced topics relating to the functional properties of HEA's. This section will be largely based on the fantastic description of HEAs in "High-Entropy Alloys - Fundamentals and Application" and the references therein, it's an excellent read. This section is particularly based on chapters 1,2,3, and 7 [1], [2], [3], [4]

2.1 Fundamentals

High-Entropy Alloys are a quickly emerging field in materials science due to the infinitely many possibilities and the unique properties. From the original discovery by Jin in 2004, as of 2015 there have been over 1000 published journal articles on high-entropy alloys. In its simplicity, a high-entropy alloy can be compared to a smoothie. By combining an assortment of fresh fruit and vegetables one can produce unique combinations of flavors and nutritional values based on both the properties of the distinct items, and their interplay in the mixture. In materials science, this exact procedure can be applied to generate a large range of materials with tunable properties depending on the intended application. In the topic of HEA's, this can be increased strength or ductility, corrosive resistance or lowered thermal conductivity, all of which have been observed in actual high-entropy alloys. Moving on from the rather banal fruit analogy, a high-entropy alloy typically falls under the two conditions.

1. The material consist of at least 5 distinct elements, where each element contribute between 5-35% of the composition
2. The total configurational entropy is greater than $1.5R$, where R is the gas constant.

The latter is an especial case for high-entropy alloys. The ideal configurational entropy of random N-component solid-solution is given in eq 2.1

$$\Delta S_{\text{config}} = -R \sum_{i=1}^N X_i \ln X_i, \quad (2.1)$$

it's clear that ΔS_{config} increase with a higher number of constituents in the mix. For instance, the ideal configurational entropy of a binary alloy is $0.69R$, while a 5-component alloy is $1.61R$. If we neglect other factors that influence the formation of solid solutions (will be covered later), from Gibbs free energy in eq 2.2

$$\Delta G_{\text{mix}} = \Delta H_{\text{mix}} - T\Delta S_{\text{mix}}, \quad (2.2)$$

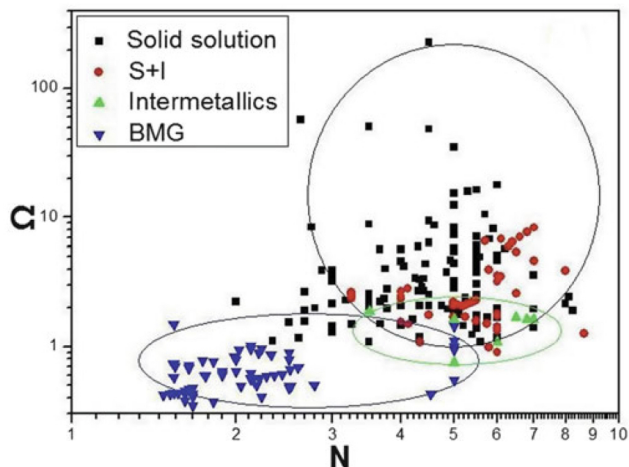
the two primary factors in formation of solid solution is the mixing enthalpy, which is the driving force to form compounds, and the mixing entropy which is the driving force to form random solid solutions. At elevated temperatures especially, the energy associated to the entropy of the system becomes comparative to the mixing enthalpy and can impact the overall equation. In summary, the overall concept of high-entropy alloys is that through alloying a greater number of elements, the gain in configurational entropy of the system prohibit the formation of intermetallic compounds in favor of a random solid solution. The random term simply relate to the various components occupying lattice positions based on probability. In fact, a narrower definition of high-entropy alloys would be structures with a single-phase disordered solid solution. The two "definitions" given previously can be considered as guidelines for the latter.

All though the mixing entropy mentioned above plays a central role in the formation, there are other factors to consider, and some that may oppose the formation of a single disordered phase. One of these is the atomic size effect which is related to the differences in atomic size, between the various elements in the alloy, this quantity is denoted δ . Y. Zhang et al. in 2008 illustrated the relationship between ΔH_{mix} and δ . When δ is very small, ie similar atomic sizes. The elements have an equal probability to occupy lattice sites to form solid solutions, but the mixing enthalpy is not negative enough to promote formation of solid solution. Increasing δ does result in greater ΔH_{mix} , but leads to a higher degree of ordering. **Include figure?** To summarize the illustration, the formation of solid solution high-entropy alloys occur in a narrow range of δ value that satisfy both the enthalpy of mixing and the disordered state. Recently, Yang and Zhang proposed the parameter Ω to evaluate the stability of high-entropy alloys. The quantity is a product of the melting temperature T_m , mixing entropy and mixing enthalpy in the following manner

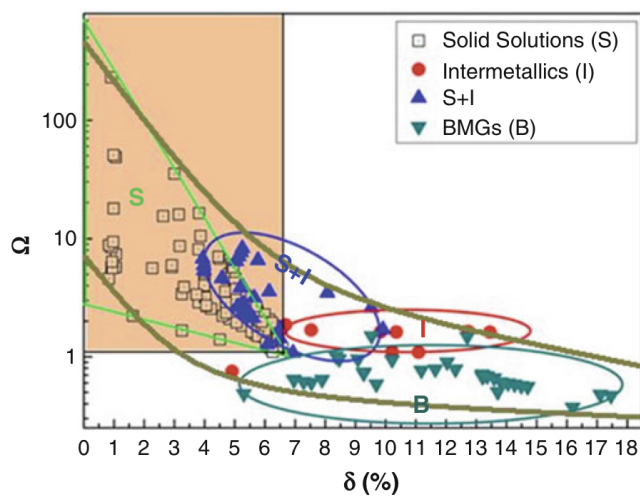
$$\Omega = \frac{T_m \delta S_{\text{mix}}}{|\Delta H_{\text{mix}}|}. \quad (2.3)$$

They managed to obtain a qualitative condition for formation of the single disordered solid solution at $\Omega \geq 1.1$ and $\delta \leq 6.6\%$. While compounds such as intermetallics form for greater values of δ and lesser values of Ω . Similarly, replacing the atomic size effect constant for the number of elements result in an equivalent condition. The results are summarized in figure 2.1

An important quantity in terms of characterizing high-entropy alloys is the total number of electrons VEC. The valence electron concentration of



(a) HEA formation based on Ω and δ



(b) HEA formation based on Ω and N

Figure 2.1: Formation of HEA based on δ and N . Figures adopted from [2]

a material is strongly related to the crystal structure of the material. For example, Co_3V , originally a hexagonal structure can be transformed into a tetragonal or cubic structure by either increasing the VEC from alloying with Ni, or reduction with Fe respectfully. Derived from the work of Guo et al. on the phase stability of a $Al_xCrCuFeNi_2$ HEA, the VEC can be directly related to the crystal structure of high-entropy alloys. A lower VEC stabilize the BCC phase, while higher values stabilize FCC. In between is a mixture of the two. Specifically values greater than 8.0 stabilize FCC, and values below 6.87 favor BCC. However, these boundaries is not rigid when including elements outside of transition metals, exceptions has also been found for high-entropy alloys containing Mn . All though a heavy majority of reported high-entropy alloys that form solid solutions have been found to adopt simple cubic structures such as FCC and BCC. Recent studies have observed HEA's in orthorombic structures like $Ti_{35}Zr_{27.5}Hf_{27.5}Ta_5Nb_5$ and hcp structures, for example $CoFeNiTi$.

2.2 Core effects and properties

Next, we will summarize the discussion above into four core effects of high entropy alloys coupled with the unique properties observed in HEAs. The first of these is called the "high-entropy effect", as explained in the previous section the configurational entropy of HEAs is much greater than in traditional solids or even binary alloys, this quantity is central to stabilize the disordered phase ahead of intermetallic or strongly ordered structures. Thus this effect can result in enhanced strength and ductility. From considerations of Gibbs free energy (Eq. 1), we see that this effect is most prominent at elevated temperatures.

The second effect is the "severe lattice distortion effect" that arises from the fact that every element in a high-entropy structure is surrounded by non-homogeneous elements, thus leading to severe lattice strain and stress. The overall lattice distortion is additionally attributed to the differences in atomic size, bonding energies and crystal structure tendencies between the components. Therefore the total lattice distortion observed in HEA's are significantly greater than that of conventional alloys. This effect mostly affect the strength and conductivity of the material, such that a higher degree of distortion yields greater strength and greatly reduces the electronic and thermal conductivity due to increased electron and phonon scattering. An upside to this is that the scattering and following properties become less temperature dependent given that it originates from the lattice rather than thermal vibrations.

The two remaining effects, "sluggish diffusion" and "cocktail effect" can be summarized swiftly. The first is a direct consequence of the multi-component layout of high-entropy alloys that result in slowed diffusion and phase transformation because of the number of different elements that is demanded in the process. The most notable product from this effect is an increased creep resistance. Lastly we have the cocktail effect, which is identical to the smoothie analogy mentioned previously, in that the

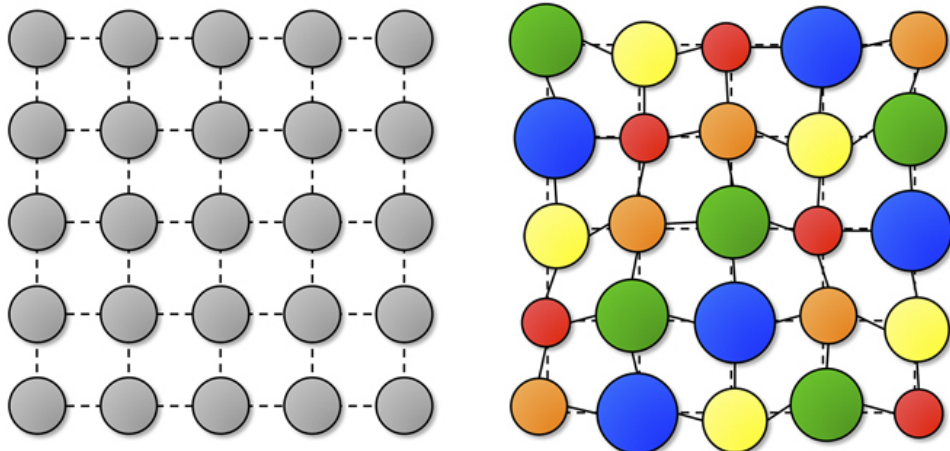


Figure 2.2: A schematic illustration of lattice distortion in high-entropy alloys. Figure from [5]

resultant characteristics is a combination of both the elements and their interaction. This is possibly the most promising concept behind high-entropy alloys, which fuels researchers with ambition to discover highly optimized materials by meticulously combining and predicting properties from different elements. Examples of this can be the refractory HEA's developed by "Air Force Research Laboratory" severely exceeding the melting points and strength of previous Ni or Co-based superalloys by alloying specifically refractory elements such as Mo, Nb and W. Another example is the research conducted by Zhang et al. on the high-entropy system $\text{FeCoNi}(\text{AlSi}_x)$ with $(0 < x \leq 0.8)$. In this HEA it was found that increased amount of either Al or Si lowered the saturation magnetization of the alloy. By tuning the relative amounts, it was found excellent properties for an $x = 0.2$ HEA in terms of the magnetization, electrical resistivity and yield strength to produce a promising soft-magnet. The same was also found in $\text{Al}_{0.2}\text{CoCrFeNi}$ where the larger addition of Ni reduced the ferromagnetism of the alloy and in CoCrCuFeNiTi_x alloys where $x = 0$ was paramagnetic and $x > 0.8$ showed superparamagnetic properties. In general we find that that the saturation magnetism is mostly dependent on the contents and distribution of ferromagnetic elements such as Fe, Co and Ni while the addition of anti-ferromagnets like Cr could be difficult to predict. For example addition of Cr to FeCoNi, the ferromagnetic compound becomes paramagnetic.

More on applications and properties?

Chapter 3

Modeling of random alloys

The structure of high-entropy alloys in which the alloying elements occupy lattice sites by a random probability pose a problem on the numerical methods used for modeling. DFT in particular rely heavily on the periodicity in crystalline solids, as we will discover later. In a brute force approach, this could be solved by randomly distribute the solute and solvent atoms over the lattice sites of a large supercell and average the energy and related properties of a great number of such supercells with varying distributions. Obviously this approach is rather efficient or even doable considering the computational demand. Thankfully today there exists a number of possible methods to more efficiently study such structures. Examples are the virtual crystal approximation (VCA), Coherent Potential approximation (CPA), special quasi-random structure (SQS), and hybrid monte-carlo/molecular dynamics. (MC/MD). A brief review of the different models is given in for example [6]. In this project we will employ the SQS method, due to both it's easy to use implementation and interpretation in VASP compared to the other options, and other benefits that will become clear after the following sections.

3.1 The Special Quasi-random Structure model

In the original paper on SQS published in 1990 [7], it was proposed a selective occupation strategy to design special periodic quasi-random structures that exceeded previous methods in both accuracy and cost. The key concept was to create a periodic unit cell of the various components in a finite N lattice site single configuration such that the structure most closely resemble the configuration average of an infinite perfect random alloy. In an attempt to work withing the 50 lattice sites boundary of ab initio methods at that time. The working theory was that if one can resemble an infinite perfect random alloy by a periodic finite N cell, also the electronic properties would be similar between the two. The solution to this model was that for each N , ie lattice site, to minimize the difference of structural correlation function between the approximated cell and the perfect random alloy. There are obviously errors involved with approximating a random alloy by a periodic cell, but by the hierarchical relation to the properties of

the material, interactions between distant sites only offer a negligible small contribution to the total energy of the system. Thus the aim of the SQS method is focused around optimizing the correlations within the first few shells of a given site. To follow is a review of the mathematical description of special quasi-random structures.

3.1.1 Mathematical description

We begin this section by giving a brief review of topics such as cluster expansions, statistics and superposition of periodic structures. A broader description of these topics can be found in the original article, or elsewhere in the literature. On a side note regarding the following mathematical derivation, the original concept was devolved in mind of an random binary alloy, but the theory have late successfully been extended to multi-component alloys and other special cases.

The different possible atomic arrangements are denoted as "configurations" σ . The various physical properties of a given configuration is $E(\sigma)$, and $\langle E \rangle$ is the ensemble average over all configurations σ . In practice, this quantity is unfeasible in terms of computational cost, seeing as the average require calculations and relaxations of all possible configurations, for a binary alloy this is 2^N for a fixed N number of lattice sites. A solution to this is to use the theory of cluster expansions and discretize each configuration into "figures" f . A figure in the lattice is defined in terms of the number of atoms it include k , distance in terms of neighbors m , and position in the lattice l . Further we assign spin values for each lattice site i in the figure to denote which element it holds (+1,-1 for a binary alloy). By defining the spin product of spin variables in a figure at lattice position l as $\Pi_f(l, \sigma)$, we can write the average of all locations in the lattice of a given figure f as

$$\Pi_f(\sigma) = \frac{1}{ND_f} \sum_l \Pi_f(l, \sigma) \quad (3.1)$$

where D_f is the number of equivalent figures f per site. The brilliance of this notation is that we now can express the physical property $E(\sigma)$ in terms of the individual contributions ϵ_f of a figure f .

$$E(\sigma) = \sum_{f,l} \Pi_f(l, \sigma) \epsilon_f(l) \quad (3.2)$$

The quantity ϵ_f is called the "effective cluster property" and is defined as (for a random binary alloy $A_{1-x}B_x$)

$$\epsilon_f(l) = 2^{-N} \sum_{\sigma}^{2^N} \Pi_f(l, \sigma) E(\sigma) \quad (3.3)$$

Inserting the equation for Π_f into that of $E(\sigma)$ we can describe the the previous cluster expansion of $E(\sigma)$ as

$$E = N \sum_f D_f \langle \Pi_f \rangle \epsilon_f \quad (3.4)$$

And obtain a simplified expression for $\langle E(\sigma) \rangle$ in eq 1? Thus we have successfully managed to reduce the expensive task of sampling all $E(\sigma)$ into calculating the effective cluster properties and summing over all types of figures. Remembering that $E(\sigma)$ can relate to many physical properties, the most common and applied case is that $E(\sigma)$ is the total energy, while ϵ_f is many body interaction energies. The cluster expansion above converge rather quickly with increasing number of figures, an effective method is thus to select a set of configurations to evaluate the effective cluster properties. Don't know how to write this, but the next step is to select a finite largest figure denoted F , and "specialize" the cluster expansion to a set of N_s periodic structures $\sigma = s$ to obtain the two expressions for $E(s)$ and ϵ_f using matrix inversion to obtain the result for ϵ_f

$$E(s) = N \sum_f^F D_f \Pi_f(s) \epsilon_f \quad (3.5)$$

$$\epsilon_f = \frac{1}{ND} \sum_s^{N_s} [\Pi_f(s)] - 1E(s) \quad (3.6)$$

Assuming now that the sum of figures F and N_s periodic structures are well converged, $E(\sigma)$ can be rewritten as a superposition of $E(s)$

$$E(\sigma) = \sum_s^{N_s} \xi_s(\sigma) E(s) \quad (3.7)$$

$$\xi_s(\sigma) = \sum_f^F [\Pi_f(s)]^{-1} \Pi_f(\sigma) \quad (3.8)$$

where ξ is the weights. Thus we have effectively reduced the problem to a convergence problem of the number of figures F and structures N_s . This can be easily solved given that we are dealing with periodic crystal structures s that can employ the general applications of ordered structures from ab initio methods, and increasing F until the truncation error falls below a desired threshold. However, this approach requires that the variance of the observable property is much lower than the sample mean, otherwise one would have to employ a much bigger sample size to reach statistical convergence. Don't know how to write this part nicely, but: Because of the different relationship between various physical properties and the correlation functions, one observe different convergence depending on the meaning of E . The idea behind SQS was therefore to design single special structures with correlation functions $\Pi_f(s)$ that most accurately match those of the ensemble average of a random alloy $\langle \Pi_f \rangle_R$.

The correlation functions of a perfect random infinite alloy, denoted as R is defined below

$$\Pi_{k,m}(R) = \langle \Pi_{k,m} \rangle_R = (2x - 1)^l \quad (3.9)$$

with k, m defined as before and x being the composition ratio of the alloy. In the case of an eqvimolar alloy ($x = \frac{1}{2}$), the functions equal 0 for all k

except $\langle \Pi_{0,1} \rangle_R = 1$. If we now randomly assign either atom A or B to every lattice site, for a sufficiently large value of N, the goal is then to create a single configuration that best match the random alloy. Keeping with the $x = \frac{1}{2}$ case, the problem is now that even though the average correlation functions of a large set of these structures approaches zero, like for the random alloy. The variance of the average is nonzero meaning that a selected structure of the sample is prone to contain errors. The extent of these errors can be evaluated from the standard deviations

$$\nu_{k,m}(N) = | \langle \Pi_{k,m}^2 \rangle |^{\frac{1}{2}} = (D_{k,m}N)^{-\frac{1}{2}} \quad (3.10)$$

Given the computational aspects, it's obvious that economical structures with small N are prone to large errors. In fact, in some cases these errors can result in correlation functions centering around 1, as opposed to 0 for a perfect random alloy.

I don't know how to write the prelude to this part! (see section IIIA in [7]). The degree to which a structure s fails to reproduce the property E of the ensemble-averaged property of the random alloy can be described by a hierarchy of figures, see eq .. bellow

$$\langle E \rangle - E(s) = \sum'_{k,m} D_{k,m} [(2x - 1)^k - \Pi_{k,m}(s)] \epsilon_{k,m} \quad (3.11)$$

, the prime is meant symbolize the absence of the value 0,1 for k,m . The contribution from the figure property ϵ reduces for larger figures. In general, for disordered systems, the physical property "E" at a given point R falls off exponentially as $|R - R'|/L$, where L is a characteristic length scale relating to the specific property. Using this, the approach of SQS is to specify a set of correlation functions that hierarchically mimic the correlation functions of the random alloy. Meaning that it prioritize the nearest neighbor interactions. With the set of functions decided on, the objective it finally to locate the structures that correspond to the selected structures.

With this approach, [7] managed by mimicking the correlation functions exact for the first two shells, to reduce the computational measures of an accurate models. In this exact study they matched the results of an $N \rightarrow \infty$ by an $N = 8$ SQS. In the final section of this chapter, we will take a look at the recent advances in the SQS method and application to high-entropy alloys.

3.1.2 Applications to high-entropy alloys

The success of the SQS method is in large part related to the fact that we can create simple periodic structures, this allows for the use of standard DFT methods to calculate with ease properties such as the total energy, charge density and electronic band structure [8], [9]. However, some certain obstacles arise when trying to apply the SQS model to high-entropy alloys. An exhaustive analysis discussing several of these factors

and comparing to alternative methods were performed in 2016 by M.C Gao et al. [10] in the framework of DFT and VASP.

The first initial concern is the size of the supercell. This parameter needs to be balanced between accuracy and cost. A larger SQS cell consisting of a greater number of atoms better encapsulate the disordered structure of HEAs, but both the generation and simulation of such large SQSs come at an increased computational demand. M.C Gao discovered a significant sensitivity between the registered stability and predicted crystal structure of CoCrFeNi and CoCrFeMnNi HEAs and varying SQSs sizes. Experimentally both of these is found stable in the FCC structure. By calculating the enthalpy of formation, he found that SQSs under 64 atoms wrongly predicted the HCP structure as the most stable, while larger SQSs correctly agreed on the FCC structure. Additionally, the probability distribution functions (PDFs) of the respective SQSs display a dependence to the SQS size. For example in 3 SQSs of size 20, 125 and 250 atoms each of FCC CrFeMnNi, the Cr-Mn is much better represented in the large SQS model as seen bellow in figure 4.1.

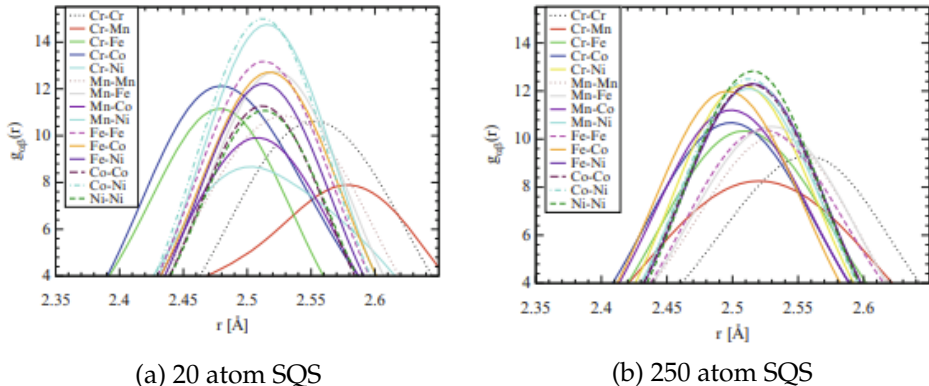


Figure 3.1: PDFs of (a) 20 and (b) 250 atom SQS models of CrFeMnNi [10]

It can also be noted that a similar dependence on the SQS size is apparent for the entropy and mechanical properties, however these topics are not relevant for this project and will thus not be elaborated further. Below we summarize the findings of M.C Gao et al between the SQS model and the crystal potential approximation and hybrid monte-carlo/molecular dynamics applied to high-entropy alloys. The comparison of SQS and MC/MD in terms of the calculated density of states can be seen in figure 3.2.

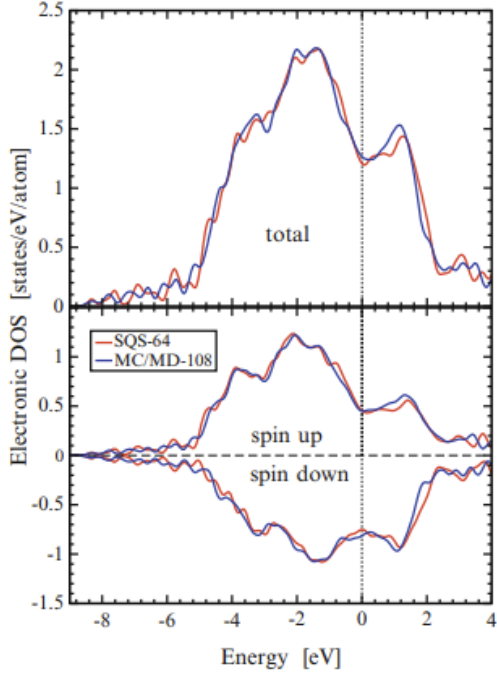


Figure 3.2: Density of states with SQS and MC/MD of FCC CoCrFeNi, figure from [10]

The density of states (DOS) of the MC/MD simulations were conducted on a larger 108 atom cell, compared to a 64 atom SQS. In despite of both the larger cell and much more complex calculations, the results of the SQS model measures up well. Furthermore, the SQS model produce a comparative outcome of the probability distribution functions (PDFs) to MC/MD as seen bellow.

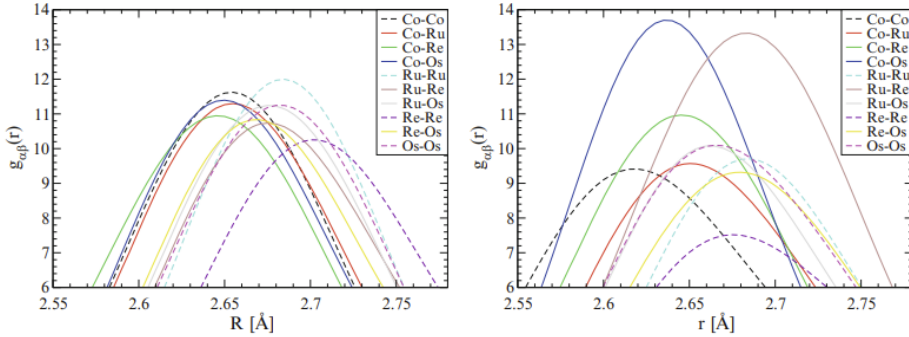


Figure 3.3: Probability distribution functions with SQS and MC/MD of HCP CoOsReRu [10]

The discrepancy in the PDFs are seen as more accurate from MC/MD calculations compared to experimental values. This is because SQS fail to include inter-atomic interaction and preference to the same extent as MC/MD. This is illustrated in figure 3.3 for the HCP CoOsreRu alloy, in which clear preference of Co-Os and Re-Ru pairs is apparent from MC/MD

simulations but not in the SQS model. Regardless, the results of SQS is very good considering the simplicity of the model and implementation. Compared to the CPA method, SQS is the less equipped method for dealing with specific cases such as $A_1/{}_3BCDE$ structures, and paramagnetic materials [10]

We have seen up until this point that the SQS method utilized an intelligent approach which allows for a simple implementation and calculations while providing results mostly on par to other more intricate and complex solutions to model disordered structures. However one particular factor concerning SQS that does not apply for CPA and MC/MD, is that within the SQS model one material can obtain in a number of distinct configurations. For example a quaternary and quinary alloy make for 24 and 124 unique configurations respectively, resulting in an uncertainty of the energy regarding the different permutations. This effect is most prominent in anisotropic lattices such as HCP and alloys with chemically dissimilar constituents, and particularly in small SQS cells [10].

Despite of it's flaws, especially in recent years SQS have emerged as a viable and trusted method of modeling disordered structures such as HEA. This is down to both the increasingly available computational power and improvements to the SQS method. The latter particularly saw a boost in 2013 with the introduction of the MC-SQS method [11], short for Monte-Carlo Special Quasirandom Structures. Contrary to the original SQS method that seek to minimize the difference between the correlation functions of the approximated cell and the true random alloy, this method employ monte-carlo simulations to perfectly match a maximum number of correlation functions. Furthermore emphasizes an efficient and fast implementation in addition to an exhaustive unbiased search of possible atomic configurations. Following, this is the preferred and most widely used method of choice in today's research, specific details on the method can be found in [11]. **How much detail do I need to include here, should I do a full explanation of the method or does this suffice?** This has resulted in an increased number of studies utilizing SQSs to investigate high-entropy alloys [12], [13], [14], and [15].

Chapter 4

Density Functional Theory

The density functional theory (DFT) is recognized as a overwhelmingly successful and important theory in quantum chemistry and the overall study and understanding of matter. As illustrated in figure 5.1 this is a increasingly popular method with rapid growth to this day due to improvements to both the method and computational power.

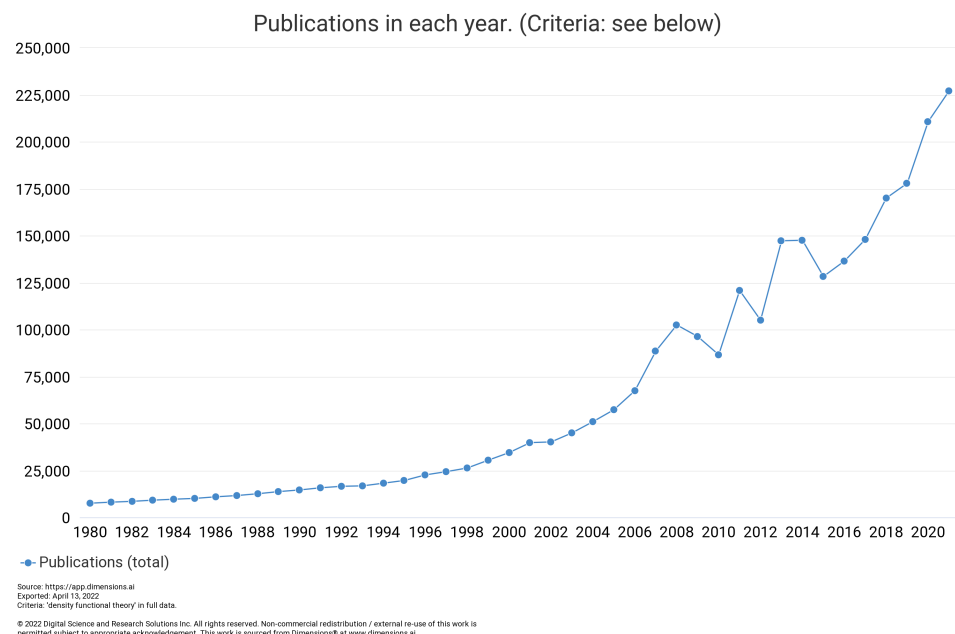


Figure 4.1: Number of DFT studies per year from 1980 to 2021 [16].

The overarching goal of DFT is to efficiently and accurately solve the many-body Shrodinger equation. Thus the this chapter will begin by refreshing some central concepts of quantum mechanics such the Shrodinger equation and the various approximations one can apply. Then we will introduce the main philosophy and idea behind both the original density functional theory and the complete Kohn-Sham density functional theory used today. Finally we will look at some of the drawbacks of DFT.

The content in this part is based on the lecture notes [17] from the course FYS-MENA4111 - "Quantum Mechanical Modelling of Nanomaterials" at the University of Oslo, written by Clas Persson. Additionally the book "A practical introduction to DFT" (Sholl, Steckel) [18]. A more elaborate description of the quantum mechanical concepts covered in this section can be found in sources such as "Introduction to quantum mechanics" by Griffiths [19].

4.1 Review of Quantum Mechanics

4.1.1 The Shrodinger equation

All theoretical information of a material can be derived from the Shrodinger equation, which came to the world in 1926. Since this the major question how been how this equation can be solved. The time-dependent Schrödinger equation for one electron is given bellow

$$i\hbar \frac{\partial}{\partial t} \Psi(\mathbf{r}, t) = \hat{H}(\mathbf{r}, t) \Psi(\mathbf{r}, t). \quad (4.1)$$

This equation consists of the the wavefunction $\Psi(\mathbf{r}, t)$ which describe the electron, and the Hamiltonian $\hat{H}(\mathbf{r}, t)$ where \mathbf{r} and t is the spatial position and time respectively. The Hamiltonian describes the systems total energy by a kinetic part $T = \frac{-\hbar^2 \nabla^2}{2m_e}$, where m_e is the electron mass and \hbar is the constant, and a potential energy operator U , typically an external potential denoted $V_{ext}(\mathbf{r}, t)$. Wavefunctions of stationary states are eigenfunctions of the Hamiltonian and are denoted as $\psi_\kappa(\mathbf{r}, t)$ with an energy eigenvalue ϵ_κ . The subscript κ indicate that the wavefunction correspond to the κ eigenstate. Above we included the time-dependent Shrodinger equation, but almost all cases involving Quantum physics employ rather the time-independent Shrodingier equation in which the external potential is independent of time. Bellow we show the time-independent Shrodinger equation for the eigenvalues E_k of the k -th eigenfunction $\psi_k(\mathbf{r})$

$$\left(-\frac{\hbar^2 \nabla^2}{2m_e} + V_{ext}(\mathbf{r}) \right) \psi_\kappa(\mathbf{r}) = E_k \psi_\kappa(\mathbf{r}) \quad (4.2)$$

Solving the single electron time-independent equation often results in infinite eqienstates that the electron can occupy. The most probable state the electron occupy is the lowest energy state called the ground state, this state is indicated by $\kappa = 0$. Extending to a system comprised of multiple particles we have the many-body Shrödinger equation with the many-body wavefunction

$$\Psi^{en}(\mathbf{r}, \mathbf{R}) = \Psi^{en}(\mathbf{r}_1, \mathbf{r}_2, \dots, \mathbf{r}_{N_e}, \mathbf{R}_1, \mathbf{R}_2, \dots, \mathbf{R}_{N_n}), \quad (4.3)$$

where r_j denote the coordinates of the j :th electron and likewise R_α describe the coordinates of the α :th nucleus, and the subscript "en" subscript

means that we consider both the electrons and nuclei. Furthermore we have the many-body Hamiltonian H^{en} , composed of the kinetic energy of N_e electrons T_e , the interaction energy between electrons U_{ee} , the kinetic energy of N_n nuclei, the coulomb interaction between nuclei U_{nn} , and finally the attractive interaction between nuclei and electrons U_{en} . In the many-body Hamiltonian the following notations are used m_n = nuclei mass, q = particle charge, α = nuclei number, Z_α = atom number of nuclei α . In final we get

$$\hat{H} = T_e + T_n + U_{ee} + U_{nn} + U_{en} \quad (4.4)$$

$$\begin{aligned} &= -\sum_{j=1}^{N_e} \frac{\hbar^2 \nabla_j^2}{2m_e} - \sum_{\alpha=1}^{N_n} \frac{\hbar^2 \nabla_\alpha^2}{2m_n} + \sum_{j=1}^{N_e} \sum_{j' < j} \frac{q^2}{|r_j - r_{j'}|} \\ &\quad + \sum_{\alpha=1}^{N_n} \sum_{\alpha' < \alpha} \frac{q^2 Z_\alpha Z_{\alpha'}}{|R_\alpha - R_{\alpha'}|} - \sum_{j=1}^{N_e} \sum_{\alpha=1}^{N_n} \frac{q^2 Z_\alpha}{|r_j - R_\alpha|}, \end{aligned} \quad (4.5)$$

and the many body Schrodinger equation with total energy eigenvalue E_κ^{en} of the whole system in eigenstate κ

$$H^{en} \Psi_\kappa^{en}(\mathbf{r}, \mathbf{R}) = E_\kappa^{en} \Psi_\kappa^{en}(\mathbf{r}, \mathbf{R}). \quad (4.6)$$

4.1.2 Approximations to the many-body Shrodinger equation

The first step to solving the many-body problem is to obtain an exact expression for the many particle wavefunction $\Psi^{en}(\mathbf{r}, \mathbf{R})$ in order to apply the single-particle operators in equation (5.4). If we consider a simplified system consisting of just two electrons, the problem is reduced to finding $\Psi_\kappa(\mathbf{r}_1, \mathbf{r}_2)$ that is a function of $\psi_1(\mathbf{r}_1)$ and $\psi_2(\mathbf{r}_2)$. In the Hartree approach this is solved by assuming that the two electrons are independent of each-other and employ variable separation to express the two particle wavefunction as

$$\Psi_\kappa(\mathbf{r}_1, \mathbf{r}_2) = \psi_1(\mathbf{r}_1) \psi_2(\mathbf{r}_2). \quad (4.7)$$

The flaw of the Hartree approach is that the electrons, which are fermions, in this formulation are distinguishable and hence does not obey the Pauli exclusion principle of fermions. This is corrected by the Harte-Fock approximation which introduces a spin function $\chi_{mp}(s_1, s_2)$ to equation (5.4) to make it anti-symmetric with respect to the particle coordinates. The Hartree-Fock approximation is expressed as

$$\Psi_\kappa(\mathbf{r}_1, \mathbf{r}_2) = \frac{1}{2} \{ \psi_1(\mathbf{r}_2) \psi_2(\mathbf{r}_2) \pm \psi_1(\mathbf{r}_2) \psi_2(\mathbf{r}_1) \} \chi_{\mp}(s_1, s_2). \quad (4.8)$$

The difference in energy from the improved wavefunction in Harte-Fock compared to the Hartee approximation is called the exchange energy. Note however that Hartee-Fock is not a complete description either as it fails to model the electron correlations. For the next step in the derivation

of the Kohn-Sham density functional theory we need to make use the variational principle. This is an efficient method for finding the ground state properties of a system. The method states that the energy of any trial wavefunction will always be higher than the ground-state energy E_0 , ie

$$E_0 = \langle \psi_0 | H | \psi_0 \rangle \leq \langle \psi | H | \psi \rangle = E \quad (4.9)$$

This enable us to find the ground state energy and corresponding wavefunction by a minimization technique. We will apply the variational principle to find the ground state energy $\Psi_0(\mathbf{r}_1, \mathbf{r}_2)$ of a two electron Hartree problem. Here we skip the derivation and mechanism behind the variational principle and simply state the final product. In final, the Hartree single-electron equation is defined as

$$\left[-\frac{\hbar^2 \nabla^2}{2m_e} + V_H(\mathbf{r}) - V_{SI}(\mathbf{r}) + V_{ext}(\mathbf{r}) \right] \psi_j(\mathbf{r}) = \epsilon_j \psi_j(\mathbf{r}), j = 1, 2. \quad (4.10)$$

Furthermore the total energy can be calculated by

$$E = \sum_j \epsilon_j - \frac{1}{2} \int (V_H(\mathbf{r}) - V_{SI}(\mathbf{r})) n(\mathbf{r}) d\mathbf{r}. \quad (4.11)$$

In the above expressions V_H and V_{SI} are the Hartree potential and the self-interaction potential respectively. The self-interaction potential is subtracted in the equations to account for that an electron can not interact with itself. The above statements can also be applied for Hartree-Fock systems and is easily extended to a N_E electron problem by setting j in Eq. (5.4) equal to $j = 1, 2, \dots, N_e$. In this case it's common to also include the self-interaction term to simply the calculations by making the total potential in Eq. (5.10) equal for all electrons, however this introduces a self-interaction error in the approximation. Moreover, by employing the variational principle, the many body equation has been transformed to a set of single electron equations, however the use of the variational principle means that this expression is valid only for the ground state.

A second essential approximation to the many-body equation is the Born-Oppenheimer approximation. This makes a very cleaver assumption that significantly simplify the equation. Given that the electron mass is negligibly small in comparison to that of a nuclei, we can treat the nuclei as point charges, enabling us to divide the eigenfunction into a separate electronic and nuclear part, in other words

$$\Psi_k^{en}(\mathbf{r}, \mathbf{R}) \approx \Psi_k(\mathbf{r}, \mathbf{R}) \Theta_k(\mathbf{R}), \quad (4.12)$$

where $\Psi_k(\mathbf{r}, \mathbf{R})$ is the electronic part and $\Theta_k(\mathbf{R})$ the nuclear part. The \mathbf{R} dependence in $\Psi_k(\mathbf{r}, \mathbf{R})$ originate from the fact that electrons can respond instantaneously to updated positions of the nuclei. Writing this in terms of the Hamiltonian give

$$(T_e + U_{ee} + U_{en}) \Psi_k(\mathbf{r}, \mathbf{R}) = E_k(\mathbf{R}) \Psi_k(\mathbf{r}, \mathbf{R}) \quad (4.13)$$

$$(T_n + U_{nn} + E_k(\mathbf{R})) \Theta(\mathbf{R}) = E_k^{en}(\mathbf{R}) \Theta_k(\mathbf{r}, \mathbf{R}). \quad (4.14)$$

We observe that the two sections are interrelated through the electronic energy $E_k(\mathbf{R})$. Furthermore, the left hand side of the nuclear part can be simplified to $U_{nn} + E_k(\mathbf{R})$, assuming that the kinetic energy of point charges is zero.

With the Hartree, Hartree-Fock and Born-Oppenheimer approximations we are finally ready to tackle the many-body Schrödinger equation. However despite the aforementioned approximations one can apply, the many-body equation still pose a few obstacles to overcome both numerically and theoretically. The first of which is how the immense number of terms in Eq. (6) can be handled in a numerical manner. As an example, a material of volume equal to 1cm^3 contain about 10^{23} nucleus and electrons which makes for nearly 10^{40} terms to solve in Eq.(5.6). A Second and more present concern is how the many-particle wavefunction Ψ^{en} is related to the single-particle wavefunctions, and how can we operate the Hamiltonian on Ψ^{en} ? This is where the density-functional theory enters. When people mention DFT today, most of the time they mean Kohn-Sham density functional theory, that combines the concept of the original density functional theory with the Kohn-Sham equation and philosophy. These two topics will be the focus of the following sections.

4.2 Kohn-Sham density functional theory

4.2.1 Density functional theory

The density functional theory was developed by Hohenberg and Kohn in 1964 and centers around the ground-state density of a system, described as

$$n_0(\mathbf{r}) = |\Psi_0(\mathbf{r})|^2. \quad (4.15)$$

The working principles and the role of the ground-state density in DFT is outlined in two theorems known as the Hohenberg-kohn theorems [lecture notes REF]:

1. "All ground-state properties of the many-body system are determined by the ground state density $n_0(\mathbf{r})$. Each property is thus a functional $f[n]$ and the ground-state property is obtained from $f[n_0]$ ".
2. "There exists a variational principle for the energy density functional such that, if n is not the electron density of the ground-state, then $E[n_0] < E[n]$."

The major benefit of this theorem is that by applying the density to calculate the ground state properties of a system, we can significantly reduce the computational complexity of the problem. This is true seeing

as the density only concerns 3 variables x , y , and z regardless of the system compared to $3N_e$ variables in the many-particle wavefunction. Moreover the second theorem states that the exact ground state energy is the global minimum for a given potential and that the density that minimize the energy functional is the exact ground-state density. From the first theorem we can now rewrite the total energy in Eq. (13) as a functional of the density, we get

$$E[n] = F[n] + \int V_{en}(\mathbf{r})n(\mathbf{r})d\mathbf{r}, \quad (4.16)$$

where $F[n] = T[n] + U_{ee}[n]$ make up the Hohenberg-Kohn functional and $\int V_{en}(\mathbf{r})n(\mathbf{r})d\mathbf{r} = U_{en}[n]$. Note that $F[n]$ is independent of the external potential, and thus is universal for all systems.

4.2.2 The Kohn-Sham Equation

The concept of Kohn-sham density functional theory is to utilize the Kohn-Sham equation to determine the ground-state density, and then invokes the theorems of DFT to find the ground state energy. The Kohn-Sham approach begins by approximating the many-particle wavefunction by Hartree type functions, ie

$$\Psi(\mathbf{r}_1, \mathbf{r}_2, \dots, \mathbf{r}_{N_e}) = \psi_1^{KS}(\mathbf{r}_1)\psi_2^{KS}(\mathbf{r}_2)\dots\psi_{N_e}^{KS}(\mathbf{r}_{N_e}), \quad (4.17)$$

where ψ_j^{KS} are auxiliary independent single-particle wavefunctions. This means that the density can be calculated simlpy as

$$n(\mathbf{r}) = \sum_{j=1}^{N_e} |\psi_j^{KS}(\mathbf{r})|^2. \quad (4.18)$$

The idea behind the Kohn-Sham equation is to now rewrite the energy in Eq. (15) as

$$E[n] = T_s[n] + U_s[n] + U_{en}[n] + \left\{ (T[n] - T_s[n]) + (U_{ee}[n] - U_s[n]) \right\}, \quad (4.19)$$

with the "s" subscript relating to that the wavefunctions are the auxiliary wavefunctions of Eq. (ABOVE). The enclosed term in Eq. (ABOVE) is known as the exchange-correlation energy E_{xc} of the system, defined as $E_{xc}[n] = \Delta T + \Delta U$. This quantity is the engine of the Kohn-Sham approach, it contains the leftover energy between the exact energy and the energy corresponding to the simpler terms $T_s[n] + U_s[n] + U_{en}[n]$ that is possible to calculate. This means that the exchange-correlation must account for the more complex energies corresponding to the many-electron interaction, electron self-interaction and the kinetic energy part. Thus if E_{xc} is eaxct, so is the total energy. In full, we can write the energy functional as

$$E[n] = \underbrace{\sum_j \int \psi_j^{KS*} \frac{-\hbar^2 \nabla^2}{2m} \psi_j^{KS} d\mathbf{r}}_{T_s[n]} + \underbrace{\frac{1}{2} \int \int q^2 \frac{n(\mathbf{r})n(\mathbf{r}')}{|\mathbf{r} - \mathbf{r}'|} d\mathbf{r} d\mathbf{r}'}_{U_s[n]} \\ + \underbrace{\int V_{en}(\mathbf{r}n(\mathbf{r})) d\mathbf{r}}_{U_{en}[n]} + \underbrace{(T[n] - T_s[n]) + (U_{ee}[n] - U_s[n])}_{E_{xc}[n]} \quad (4.20)$$

Similar to how the single particle Hartree equation was found in Eq. (10), the Kohn-Sham single-particle wavefunction can be reached from utilizing the variational principle.

$$\left\{ -\frac{\hbar^2}{2m_e} \nabla_s^2 + v_H(\mathbf{r}) + V_{en}(\mathbf{r}) + V_{xc}(\mathbf{r}) \right\} \psi_s^{KS}(\mathbf{r}) = \epsilon_s^{KS}(\mathbf{r}) \psi_s^{KS}(\mathbf{r}). \quad (4.21)$$

With this expression it's now possible to calculate the ground state density in Eq. (17) by solving Eq. (ABOVE) for all the ground state single electron wavefunctions. Finally, we have the total energy of the system expressed as

$$E[n] = \sum_j \epsilon_j^{KS} - \frac{1}{2} \int V_H(\mathbf{r}) n(\mathbf{r}) d\mathbf{r} + E_{xc}[n] - \int V_{xc}(\mathbf{r}) n(\mathbf{r}) d\mathbf{r}, \quad (4.22)$$

where $V_{xc}(\mathbf{r}) = \frac{\partial E_{xc}[n]}{\partial n}$ is the exchange-correlation potential. This is the Kohn-Sham density functional theory.

4.3 Limitations of DFT - Insert refs

"Any fool can know. The point is to understand" - Albert Einstein

In this section we intend to outline and *understand* the fundamental drawbacks and limitations of the density functional theory in light of both the theoretical formulation and the practical aspects of performing DFT based simulations. The primary drawback of the density functional theory is that to this day we still don't have the exact form of E_{xc} . From the above derivations we recognize that this term must account for several complex properties such as the many-body interaction and large amounts of kinetic energy. Additionally the exchange-correlation must also include the self-interaction error from applying Hartree-like wavefunctions in the Kohn-Sham equation. Furthermore this functional should be applicable in any material, ie metals, semiconductors, liquids and gasses. In the next section we will look at some of the most commonly used approximations to E_{xc} . These approximate functionals range from low-complex and computationally cheap methods such as LDA, to heavy computational methods such as hybrid functionals. This is therefore seen as a disagreement

between the theoretical philosophy of the DFT and the practical application of it, ie in practice one must adapt the functional first to the type of system and intention, for example if one wants to study the band gap, or weak Wan-Der Waals interactions. Secondly the functional must be chosen as a compromise between accuracy and cost.

However, even if the exchange-correlation functional was expressed exactly and efficiently implemented, DFT would still serve a couple of drawbacks. For instance the Kohn-Sham eigenfunctions in equations 17 are not the true single-electron eigenfunctions, thus also the corresponding eigenvalues are not exact even with an exact value of E_{xc} , meaning that the band gap obtained from the eigenvalues is in nature inexact. In fact, the estimation of the band gap of semiconductors is one of the major shortcomings of DFT. In addition to the eigenvalue, the band gap is also subject to underestimation due to a self-interaction term that over-delocalize the occupied states and hence pushes them up in energy, effectively reducing the band gap [20]. More advanced topics regarding the under-estimation of the band gap in semiconductors from DFT calculations can be read about in [21], by John P. Perdew and Mel Levy. Additionally, DFT also have difficulties in simulating weak long-range Wan-der Waal attraction [22], due to DFT's emphasis on primarily the local density, thus to some degree neglect long-range effects.

More practical limitations of DFT include factors such as the calculations not being variational with respect to the functional, meaning that a more complex functional does not guarantee higher accuracy [23]. Moreover the calculations of DFT only deliver a local minimum, in other words the calculations only return the most stable energy for the given initial settings and parameters. An example of this is seen when studying magnetic materials, where the total energy of a DFT calculation vary between each magnetic configuration of the material, meaning that to obtain the true ground-state energy one must perform an exhaustive search of all magnetic possibilities. Similar is also the case when comparing crystal structures and geometric features of materials. Finally, despite the possibility of simulations of excited states exists today, DFT in its original formulation is only valid for the ground state. Thus these calculations have a lesser theoretical footing in comparison.

Regardless of its' flaws, DFT is still considered a widely successful method and accordingly Walter Kohn and John A. Pope won the Nobel prize in chemistry in 1998; "to Walter Kohn for his development of the density-functional theory and to John Pople for his development of computational methods in quantum chemistry." [24]

Part II

Methodology and Implementation

Chapter 5

Practical application of DFT

In this section we will present the practical application and implementation of density functional theory in the study of materials science.

5.1 The Exchange-Correlation functional

From the former section, we know that the one piece of information missing of the density functional theory is the complex exchange-correlation energy $E_{xc}[n]$ that must account for all the simplifications and approximations employed in Kohn-Sham DFT. In this section we will explore some of the options do include the exchange-correlation functional, they operate in 4 levels of complexity. First is the local density approximation (LDA), followed by the generalized gradient approximation (GGA). These two are the least complex and computationally affording methods of calculating E_{xc} . Next is the methods such as meta-GGA implementations and finally the very accurate, but equally demanding hybrid-functionals. We will begin this section by describing the local density approximation.

5.1.1 Local density approximation

A homogeneous electron gas (HEG) is the sole case we know of where the exchange-correlation functional can be determined exactly, because in the simple example the electron density is constant. The LDA works by setting the exchange-correlation potential $V_{XC}(\mathbf{r})$ at every position equal to that of the homogeneous electron gas, in other words

$$V_{XC}(\mathbf{r}) = V_{XC}^{\text{HEG}}[n(\mathbf{r})]. \quad (5.1)$$

Obviously the LDA is of limited use given that a large part of what makes materials interesting is the change in the electronic density, for example LDA is known to overestimate binding energies and underestimate the band gap in semiconductors and insulators. On the other hand, LDA provide generally adequate results in bulk materials with slowly varying charge density, for example equilibrium distances and vibrational frequencies. The biggest upside of LDA however comes from the low computational cost, and was one of the first big success-stories of DFT.

5.1.2 Generalized gradient approximation

A natural succession to the local density approximation is the family of generalized gradient approximation (GGA) that also include the gradient of the electron density

$$V_{\text{XC}}^{\text{GGA}}(\mathbf{r}) = V_{\text{XC}}[n(\mathbf{r}), \nabla n(\mathbf{r})]. \quad (5.2)$$

The way one can implement the gradient are plenty-full and complicated. Two of the most common methods are the Perdew-Wang 91 (PW91) [25] and the Perdew-Burke-Ernzerhof (PBE) GGA [26]. This project will utilize the latter which came to fruition in 1996 in an article by Perdew, Burke and Ernzerhof appropriately named "Generalized Gradient Approximation Made Simple". The key point regarding the PBE functional is that it's a non-empirical method thus providing reliable and adequate accuracy over a wide range of systems, as compared to for instance the BLYP functional that provide excellent accuracy of organic molecules but fails in other cases [27]. In fact, the original PBE article is the 16th most cited scholarly article of all time (as of 2004) Cite: https://www.nature.com/news/polopoly_fs/1.16224!/menu/main/topColumns/topLeftColumn/pdf/514550a.pdf, to illustrate the application and importance of this method.

5.1.3 Meta-GGA

Meta-GGA functionals is the final level of complexity of the non-empirical approximations to the exchange-correlation functional. In addition to the constant density (LDA) and local gradient of the density (GGA), meta-GGA methods consider the kinetic energy density of the occupied Kohn-Sham orbitals [28], defined as

$$\tau_\omega = \sum_i^{\text{occ}} \frac{1}{2} |\nabla_{\psi_{i,\omega}}|^2. \quad (5.3)$$

The role of this quantity on the the calculated band gap is well described in [29]. In this project we employ a meta-GGA functional named *Strongly Constrained Appropriately Normed*, or SCAN. This functional is the only known functional to satisfy all 17 known exact constraints of the XC functional [30]. The initial outcomes of the SCAN functional showed promising improvement over both LDA and PBE at similar computational cost. Studies utilizing the SCNA functional have found results supporting superior accuracy of the band gap and electronic density of states [31], and atomic structures [32]. Moreover can provide high accuracy and comparative outputs to hybrid functionals for geometries and energies in diversely bonded materials [33], compared to LDA and PBE. However drawbacks are also present in the SCAN functional, one of these is opposite to structures with strong binding where SCAN yields superior accuracy of crystal volume, magnetism and band gap, SCAN is observed less reliable and accurate to PBE in weakly-bound structures [34]. Another very popular meta-GGA implementation is the *Modified Becke-Johnson* functional

[35], however we did not manage to converge calculations with this functional in this project.

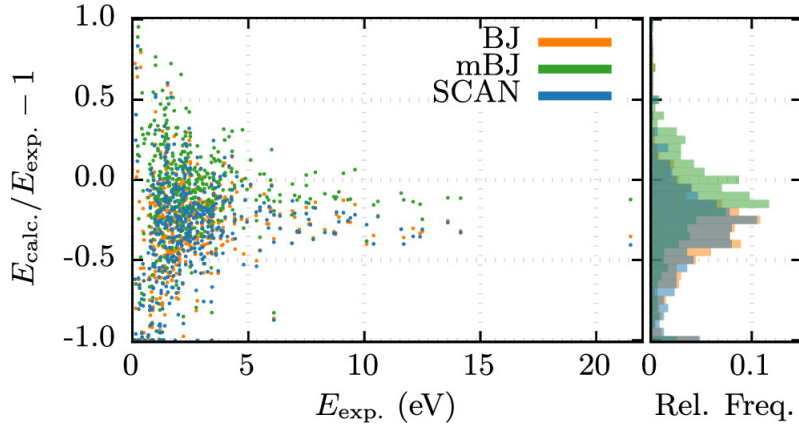


Figure 5.1: Calculated to experimental band gap measurements of Becke-Johnsoon, modified Becke-Johnson and SCAN functionals [36]

5.1.4 Hybrid functionals

The most precise functional known to DFT belong to the family of *hybrid functionals*. Accordingly this method consist of a hybrid between simpler functionals such as LDA, PBE or even meta-GGA and the exact treatment of exchange energy from Hartree-Fock, for example the global hybrid functional PBE0 [37] described as

$$E_{\text{xc}}^{\text{PBE0}} = (1 - \alpha)E_x^{\text{PBE}} + \alpha E_x^{\text{HF}} + E_c^{\text{PBE}}, \quad (5.4)$$

where alpha is the mixing parameter to decide the balance between the exchange energy, denoted x of Hartree-Fock with PBE, alike the last term represent the correlation energy from the PBE functional. This parameter alpha is determined empirically, thus making hybrid functional a semi-empirical model. Obviously considering the exact exchange in Hartree-Fock is a computationally challenging prospect. Heyd-Scuseria-Ernzerhof managed to lower the cost by the concept of Screened functionals that separate the Coloumb interaction into long-range and short-range interaction by a function $\text{erfc}(\mu r)$. These are known as HSE functionals [38], the overall best functional for accurate band gaps of solids is by many considered to be HSE06 [39] with $\alpha = 0.25$ and $\mu = 0.11$.

5.1.5 Outlook

In many cases LDA and GGA suffice, PBE especially is by most considered the conventional standard for DFT calculations, for its balance of accuracy, cost and wide range applicability. However, distinctly concerning the band gap of a solids, both of these fall short. This is because the band gap of DFT calculations is complicated by the fact that the derivative of the XC-functional is discontinues with respect to the electron concentration [40],

thus the simpler functionals fail to recall the experimental values since the total band gap in DFT is the fundamental gap (valence - conduction) + this contribution. This is corrected in meta-GGA and hybrid functionals in the generalized Kohn-Sham scheme. Lastly, we would like to refer the reader to the work of Borlido, Aull, Huran, Tran, Marques, and Botti whom in 2019 conducted an exhaustive investigation of the band gap of over 470 unique non-magnetic compounds in order to benchmark the relative performance of several of the available and widely used XC-functionals [36]. In this large-scale project they found overwhelming confirmation that the HSE06 functional followed closely by Modified-Becke Johnson is the superior choice for accurate band-gap measures. Regarding the SCAN functional, in several cases this yielded outputs very comparable to MBJ, and produce much better formation energies than PBE, but tend to overestimate in magnetic alloys. On the other hand the LDA and PBE functional resulted in 50% and 30% under-estimation of the band gap and several cases of miss-classified metals, this was particularly evident in compounds containing Ni and other 3d elements. This result in a limited application to for example narrow gap thermoelectrics or photovoltaics where accurate values of the band gap and states at the band edges is critical.

5.2 Fundamental aspects of practical DFT calculations

Needs work, see mainly DFT book ch 3 With the exchange-correlation functionals presented above, we now have everything in order to perform DFT calculations. To begin solving eq .., we need the single-electron wavefunction, for a free electron this is a plane wave $\psi_k = Ae^{ikr}$. In a solid however, there exist a nonzero periodic potential $V(\mathbf{r}) = V(\mathbf{r} + \mathbf{R})$, the solution to the Shrödinger equation is given by Bloch's theorem which states that the solution takes the form

$$\psi_k(\mathbf{r}) = u_k(\mathbf{r})e^{ikr}, \quad (5.5)$$

where $u_k(\mathbf{r})$ is a Bloch wave with the periodicity of the supercell, and k is the wavevector. Similar to eq(above), k-space, or reciprocal space is useful to solve the numerous mathematical problems posed by DFT. For instance a great deal of DFT calculations revolve around solving the integral

$$g = \frac{V_{\text{cell}}}{(2\pi)^3} \int_{\text{BZ}} g(k) dk, \quad (5.6)$$

with BZ denoting that the integral be evaluated for all k in the Brillouin zone. This integral can be approximated by evaluating the integral at a set of discrete points and summing over the points with appropriately assigned weights. A larger set of points leads to more exact approximations. This method is called Legendre quadrature. The method for selecting these points in reciprocal space was developed by Monkhorst and Pack in 1976, and simply put requires a amount of kpoints in each direction in reciprocal

space, in the form $N \times N \times N$. Recalling that reciprocal space is inverse to regular space, supercells with equal and large dimensions converge at smaller values of N , and inversely for cells of small dimension. In supercells with different length axis, such as hexagonal cells, we use the notation $N \times N \times M$, where M relate to the distinctly different axis. The amount of kpoints required can be further reduced by utilizing the symmetry of the cell, in which we can exactly approximate the entire BZ by extending a lesser zone through symmetry. This reduced zone is appropriately named the irreducible Brillouin zone (IBZ).

Metals in particular require a large set of kpoints to achieve accurate results. This is because we encounter discontinuous functions in the Brillouin zone around the fermi surface where the states discontinuously change from occupied to non-occupied. To reduce the cost of this operation, there are two primary methods, tetrahedron and smearing. The idea behind the tetrahedron method is to use the discrete set of k-points to fill the reciprocal space with tetrahedra and interpolate the function within each tetrahedron such that the function can be integrated in the entire space rather than at discrete points. The latter approach for solving discontinuous integrals is to smear out the discontinuity and thus transforming the integral to a continuous one. A good analogy to this method is the Fermi-Dirac function, in which a small variable σ transforms a step-function into a continuous function that can be integrated by standard methods.

In addition to the number of kpoints, there is one more distinct parameter that must be specified in DFT calculations, namely the energy cutoff, or E_{cut} . These parameters arise from the Bloch function described previously. In which $u_k(\mathbf{r})$ was a Bloch wave with the same periodicity as the supercell. This implies that the wave can be expanded by a set of special plane waves as

$$u_k(\mathbf{r}) = \sum_G c_G e^{iG\mathbf{r}}, \quad (5.7)$$

where G is the reciprocal lattice vector. Combining this with eq ..(first eq for Bloch function) we get

$$\psi_k(\mathbf{r}) = \sum_G c_{k+G} e^{i(k+G)\mathbf{r}} \quad (5.8)$$

The consequence from this expression is that evaluating the wavefunction of an electron at a single k point demands a summation over the entirety of reciprocal space. In order to reduce this computational burden, we can introduce a maximum parameter E_{cut} to cap the calculations. This is possible because eq ..(above) is the solution of the Schrödinger equation with kinetic energy

$$E = \frac{\hbar^2}{2m} |\mathbf{k} + \mathbf{G}|^2. \quad (5.9)$$

Seeing as the solutions with lower energies are the most interesting, we can limit the calculations of eq ..(2 above) to solutions with energy less than E_{cut} given below

$$E_{\text{cut}} = \frac{\hbar^2}{2m} G_{\text{cut}}. \quad (5.10)$$

Thus, we can reduce the infinitely large sum above to a much more feasible calculation in

$$\psi_k(\mathbf{r}) = \sum_{|\mathbf{k}+\mathbf{G}| < G_{\text{cut}}} c_{\mathbf{k}+\mathbf{G}} e^{i(\mathbf{k}+\mathbf{G})\cdot\mathbf{r}} \quad (5.11)$$

A summary on kpoints and ENCUT, plus a discussion on numerical convergence and how to select kpoints and ENCUT

A final consideration to how DFT is applied in practise is how the core electrons are handled. Tightly bound core electrons as opposed to valence electrons demand a greater number of plane-waves to converge. The most efficient method of reducing the expenses of core-electrons are so-called pseudopotentials. This method works by approximating the electron density of the core electrons by a constant density that mimic the properties of true ion core and core electrons. This density is then remained constant for all subsequent calculations, ie only considering the valence electrons while regarding the core electrons as frozen-in. There are currently two popular types of psudopotentials used in DFT, so-called ultrasoft psudopotentials (USPPs) devoplped by Vanderbilt, and the projector augmented-wave (PAW) method by Bloch [41], [42].

5.3 Self-consistent field calculation

Needs work, see lecture notes ch 8, book ch1 Preceding this section, we have considered the fundamental theory of DFT and it's practical ability to model various materials. In figure 5.2 we present the self-consistent field calculation scheme for how DFT calculations are performed. The initial problem posed by dft is that all properties rely on the density, and are dependent on each other. For instance, the effective potential is dependent on the density, which again is dependent on the eigenfunctions, that rely on the effective potential again. The cleaver approach, as seen in figure 5.2 begin with an initial guess to the density from which we can solve the Kohn-Sham equation and obtain the corresponding eigenfunctions. Following is an iterative method where we apply the recently calculated eigenfunctions to determine a new density and repeat the procedure above. This is repeated until the total energy is converged, by an own-defined criterion. Equivalently, the optimal ionic positions can be found by a similar approach. This method is based on quasi-Newton algorithms to minimize the forces between ions.

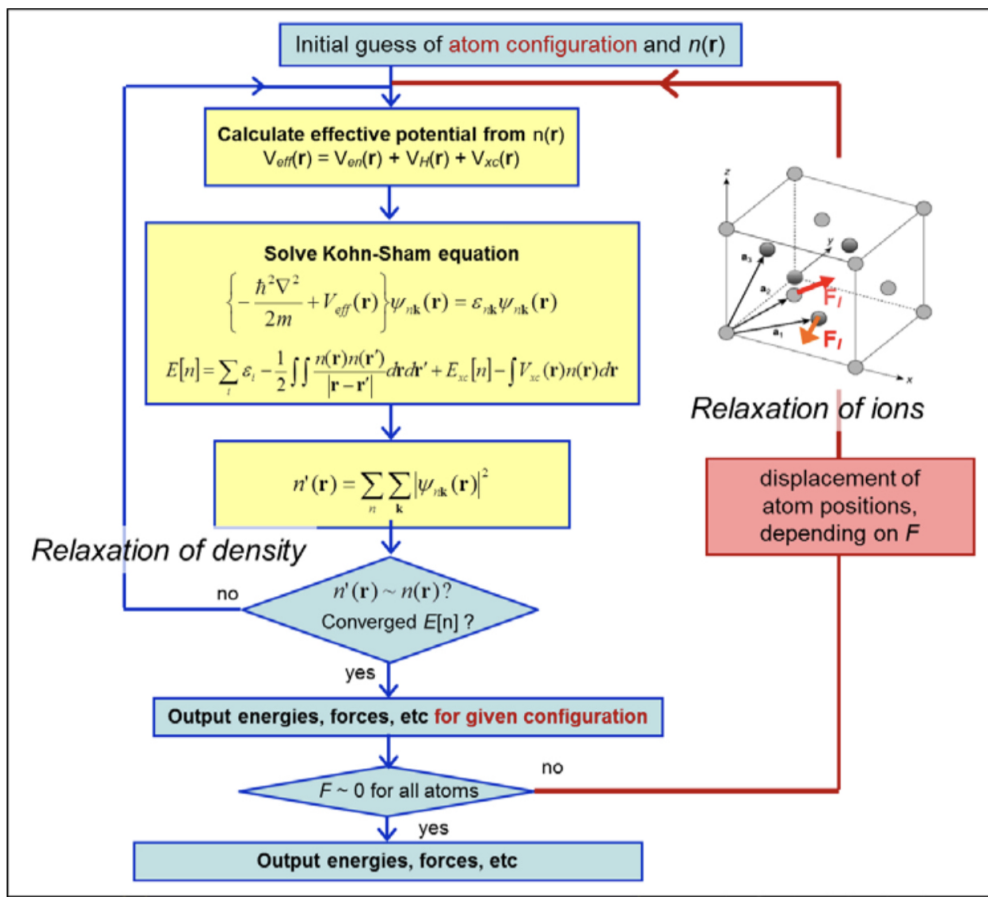


Figure 5.2: Self consistent iteration of a DFT calculation. Figure adopted from lecture notes fys-mena4111 cite

Chapter 6

Computational details

This section is intended to provide the necessary details for reproduction of results to be presented later on. First we begin by describing the software used for the project.

6.1 Vienna Ab initio Simulation Package

This software, often referred to as VASP is a package for ab initio quantum mechanics calculations using the projected augmented wave method and plane wave basis set. The intended methodology is DFT, but have been extended for methods post the original DFT-formulation. Calculations with VASP was carried out on the supercomputer fram, with allocated time and resources provided by Uninett Sigma2,[add reference!](#)

The structure of VASP rely on a set of input files and output files from the calculation, the input files required to perform a DFT computation in VASP are the following:

- INCAR - this file provide the tags responsible for different methods, algorithms, parameters etc.
- POSCAR - this file is related to the crystal structure of the system
- POTCAR - What psudopotential that is used
- KPOINTS - A file containing information on what KPOINTS will be used
- jobfile - This file contains information for the supercomputer regarding resources and such.

The capitalization displayed above is directly related to the requirements of the file system in the VASP/fram collaboration. Some important output files are:

- CONTCAR - The relaxed crystal structure after finalized calculation
- CHGCAR - This file contains the electron density after calculation

- EIGENVAL - Contains the solutions to the Kohn-Sham eigenfunctions
- DOSCAR - Information on the Density of States
- OUTCAR - Contains a list of all other information.

Some figure or tables to make this information more presentable

In this project, we used the PAW pseudopotential, and PBE GGA in favor of LDA for the reasons mentioned previously. Furthermore we readily employed meta-GGA functionals and hybrid-functionals, in particular SCAN and HSE06. We began the calculation of every individual structure by testing the convergence of total energy with respect to the number of k-points and cutoff energy. In VASP, the latter can be specified by setting the tag "ENCUT" in the INCAR file, we found 300 eV to yield productive results in terms of convergence and computation time for total energy calculations, and 400 for ionic+volume relaxations. Regarding the number of points in the reciprocal space, we carried out a great deal of simulations on numerous structures with distinct crystal structures and corresponding supercells, for this reason we employed a number of different sets of k-points depending on the structure. Typically the number of points ranged from a 2x2x2 mesh to 4x4x4 mesh. With the smaller being required for hybrid functionals to converge.

Upon realizing the convergence parameters, the structures were allowed to relax both the ionic positions, and cell volume with the quasi-newton method and a convergence criterion of $1E - 2$ for the forces and $1E - 5$ for the total energy. However, the symmetry of the structure was forced constant by the use of vasp-std-noshear. This process was repeated two times before performing final total energy calculation with various functionals.

The specific tags, algorithms, parameters and options of VASP that was in use throughout this project can be found at our GitHub address, but in particular we would like to cover two specific parameters. The First is related to the magnetic configuration of our calculations, specified with the tag ISPIN in VASP. We used ISPIN=2 which allow for co-linear spin-polarized calculations due to the involvement of ferromagnetic elements such as iron and nickel in this study. However, there are many more magnetic orientations the system can adopt besides co-linear, therefore the final total energies we found may not be the true lowest energies. But given the allocated duration and resources of this project, this is understood consequence. Secondly is the type of smearing that was used for the different calculations. The preferred method for accurate total energies and density of states in semiconductors is the tetrahedron method [43], and for accurate forces in metals the Methfessel-Paxton method is recommended. However, our system contains both metals and a large portion of Si. For this reason we used a combination of smearing methods. For the relaxation and minimization of forces, we used gaussian smearing with smearing width $\sigma = 0.05$, as this method provide accurate forces in both metallic and semiconducting materials. And to calculate the total energy and

DOS, we used the tetrahedron method, as recommended. In order to obtain converged results of the HSE06 functional, we first calculated the charge density with gaussian smearing, then apply this density to perform a second hybrid calculation with the tetrahedron method. This was necessary because gaussian smearing yielded inaccurate and unreliable results in terms of the density of states when comparing to the band gap from the koh-Sham eigenvalues. However, this method, in addition to the narrow k-grid of just 2x2x2 k-points does include a factor of uncertainty regarding these results from the HSE06 functional.

This [44] is a good reference for extracting the band gap of VASP jobs relating to smearing and DOSCAR vs EIGENVAL

Band structure/DOS and band-unfolding?

6.2 Generation of SQS

Needs work, add part on filling ratio of ideal cube The generation of special quasi-random structures as described in section .., was done by utilizing the Temperature Dependent Effective Potential (TDEP) method. This package, devolved by Olle Hellman, offers a wide range of tools primary intended for studies of finite temperature lattice dynamics. In this project we utilize the program generate-structure within the TDEP package to construct SQS's. The work of TDEP is the result of an unpublished PHD thesis by Nina Shulumba (**Insert citation**), thus the documentation on the software and generate-structure script is limited, please refer to the original author for more information.

In this project, we constructed SQS's by first transforming the cif-files of a given initial structure, for instance that of $FeSi_2$, to a primitive unit cell. The SQS's was generated by the same principles explained in section .., for each structure we created 5 distinct SQS's of an equal size under the constraint that the 3d atoms be distributed eqvimolar in the system. Precise file formats and such can be found at GitHub. Another approach could have been to construct SQS's of specific cell counts instead of total number of atoms, however this quickly lead to extremely large supercells, up to 256 atoms, that simply would not converge to our best efforts.

We began by studying high-entropy silicides by alloying 3d-metal silicides such as Fe_2Si by Cr, Fe, Co, and Ni to construct a $(CoCrFeNi)_2Si$ alloys. From this point we varied the distribution and type of elements in an attempt to locate high-entropy silicides with semiconducting properties, but remained within quaternary 3d silicides. Examples of SQSs generated by TDEP, from $FeSi_2$ structure with Cr, Fe, Mn and Ni can be seen in figure 6.1.

The $FeSi_2$ structure consisted of 48 atoms, 16 of which is iron and the remaining 32 sites occupied by silicon atoms. We filled the 16 iron sites with an even distribution of chromium, iron, manganese and nickel by the principle of the SQS method described in section .. . With this approach, there are many possible supercells one can create, we however limit ourself to 5 distinct supercells per composition, which means that we have 5

structures of the same composition and space group, but the distribution is slightly different. This allow us to both study a composition to great depth, but also to test different compositions and structures, compared to if we instead generated 10 or 15 or more supercells. But its important to be aware of this assumption, as our results may be subject to errors and result that does not match the true random alloy due to a small sample size.

6.3 Utility scripts

During the course of the projects lifetime, several shell and python scripts was developed by myself and/or provided to me by my supervisor Ole Martin Løvvik and his team of researchers at Sintef. These can be located at the GitHub address :...

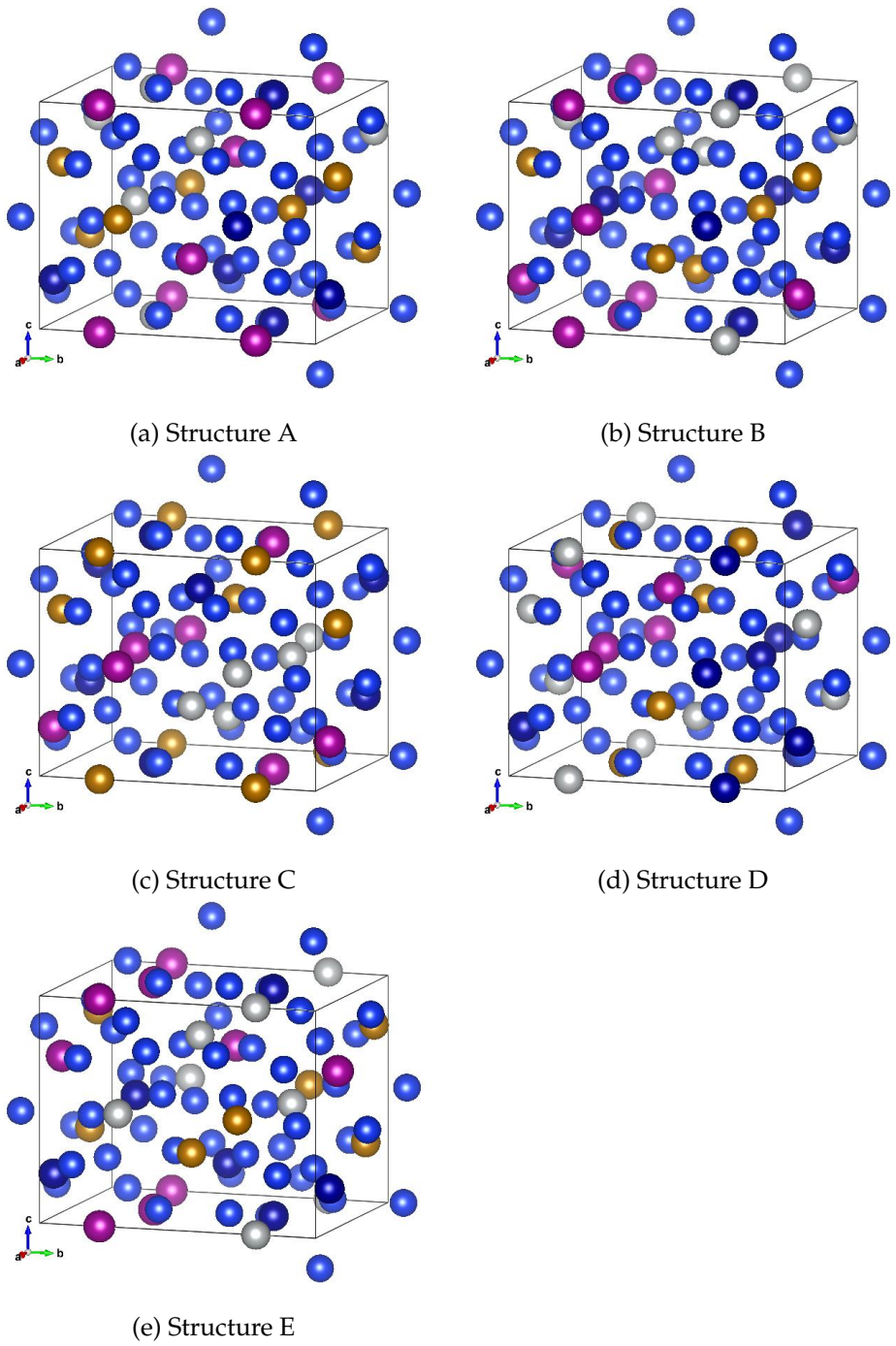


Figure 6.1: 48 atom SQS based on eqvimolar distribution of Cr, Fe, Mn and Ni in and $FeSi_2$ cell.

Part III

Results and Discussion

Change this introduction to fit the final product! In this one year long project, we have collected results of a great number of materials with various structures and compositions. The initial experimentation was based on high-entropy silicides of the Fe_2Si unit cell, created from the special quasi-random structure approach as described above. Despite the non-semiconducting character of this compound, we worked under the idea that the extraordinary properties that have been observed in high-entropy alloys through effects such as the cocktail effect, we could discover specific combinations of elements that would yield a semiconductor. In addition, the ratio between silicon atoms to metals allowed us to create nearly eqvimolar high-entropy alloys.

Following this attempt, we transitioned into studying high-entropy silicides based on well known semiconducting 3d silicides such as $\beta-FeSi_2$, $CrSi_2$ and $MnSi_{1.75}$. The main outcome of this project is that for all 4 different starting silicides, we could only produce high-entropy silicides from one unit cell, furthermore in this cell only one specific compositions of elements was semiconducting. This was $Cr_{0.25}Fe_0 \cdot 25Mn_{0.25}Ni_{0.25}Si_2$, herein CFMN, in the $\beta-FeSi_2$ crystal structure.

This section will be structured in the following manner, firstly we will investigate the CFMN (fesi2) compound and various permutations of the composition. Thereafter we will look at other possible compositions of fesi2 based high-entropy silicides, and lastly test the CFMN composition in other crystal symmetries. In final we will present an overview of the complete study and the various compounds that have been investigated in order to propose promising directions and guideline future research directions in this field. In this way, we aim to understand the unique properties of CFMN (fesi2) and why this particular compound is semiconducting compared to the other testes structures in this project. Properties we will cover is the overall stability by total energy and corresponding enthalpy of formation, the magnetic properties and which elements contribute to the magnetism. But in majority, we will look at the band gap and related properties, as this is the main motivation and distinction of the study.

Chapter 7

The results of $(\text{CrFeMnNi})\text{Si}_2$ in the $\beta-\text{FeSi}_2$ structure

$\beta - \text{FeSi}_2$ in the orthorombic cmce crystal lattice is a well known semiconductor with an experimentally measured band gap of around 0.8 ev **cite**, the nature of the band gap is under debate, all though most ab initio studies point to an indirect gap, experimental work indicate a direct gap. From our own DFT calculations, we find an indirect band gap close to 0.65 eV with PBE. This is in good agreement with other measurements from ab initio studies **cite materials projects, other studies**.

The density of states and charge density of bulk $\beta-\text{FeSi}_2$ from PBE calculations can be seen in figure .., .. From the figures we observe a clear band gap and semiconducting character. Moreover, we note from the density of states that the gap is identical in both spin channels, indicating that this material is diamagnetic. We find this to be true from the written magnetization in VASP, this also is in agreement with relevant literature **cite**. **Find reference for ΔH^0** . Finally, the enthalpy of formation of this compound is -18.6583 eV.

7.1 Eqvimolar SQSs

7.1.1 Introduction

The CFMN alloys of the fesi2 unit cell alloys can be seen in figure ... The supercells consist of 48 atoms, 16 of which is evenly distributed between Cr, Fe, Mn, and Ni, the remaining 32 sites occupied by silicon atoms. Below in table .. we list the total energy per atom (Toten), final magnetic moment per atom (Mag), and the band gap of the five distinct SQSs corresponding to the CFMN (fesi2) compound. In addition we include the mean and standard deviation of the values, plus the enthalpy of formation. For simplicity, we denote the SQSs as A, B, C, D and E.

Structure	Toten (eV)	Mag (?)	Band gap (eV)
A	-6,6080	0.0833	0.0280
B	-6,6138	0.0833	0.0523
C	-6,6063	0.0834	0.0344
D	-6,6155	0.0833	0
E	-6,6089	0.0833	0.0495
Mean	-6.6105	4.0000	0.0328
Std	0.0039	0.0000	0.0210
ΔH_{mean}^0	-11.5000 eV	-	-

Table 7.1: Total energy per atom, final magnetic moment, band gap (GGA) and formation enthalpy of $Cr_4Fe_4Mn_4Ni_4Si_{32}$ SQSs based on $FeSi_2$

Write a section on magnetism in method From a first glance, we observe very similar properties between the SQSs regarding both the total energy and final magnetic moment. Comparing to bulk $FeSi_2$, this compound is both less stable, from the enthalpy of formation, and magnetic. For the magnetic character of the compound, we performed self-consistent total energy calculations with three different magnetic configurations, non-magnetic ($ispin=1$), colinear magnetism with the initial magnetic moment equal to 1 times the number of ions, and lastly two times N ions. Of the three starting positions, we found the two latter to yield near identical total energies, with the middle setting winning out in some SQSs. The consistent magnetic moment between the 5 supercells is expected seeing as all 5 structures consist of equivalent elements. The magnetic moment observed is solely attributed from 3d electrons and in particular those of chromium and manganese atoms.

7.1.2 The band gap

The most interesting property of these SQSs is in fact the band gap. We note a mean band gap of about 0.03 eV, much lower than 0.65 eV of bulk $FeSi_2$. But a band gap in this smaller range makes for excellent application in for instance thermoelectrics. The gap is seen in 4 out of 5 SQSs, but surprisingly not in the most stable arrangement (D), the largest gap observed is about 0.05 eV from structure B, which is slightly below D in terms of total energy, but still a way above the mean energy. Similar to the bulk material, also these band gaps are indirect, the transitions are listed below in table

Structure	Gap (D/I)	Transition
A	I	(0.500,0.333,0.500) → (0.500,0.000,0.000)
B	I	(0.250,0.000,0.250) → (0.000,0.000,0.000)
C	-	(0.500,0.000,0.500) → (-0.250,0.333,0.500)
D	I	-
E	I	(0.000,0.000,0.000) → (0.250,0.000,0.250)

Table 7.2: Band gap transition of CFMN (fesi2) SQSs with PBE functional

A very useful method to extract information regarding the band gap of a material is to plot and study the band structure, however this is not as insightful when considering large supercells consisting of several elements and a large number of energy bands. The solution to this is normally to do a band unfolding, but given the complex structure and implementation of SQSs in VASP proved difficult. Instead we investigate the band gap from the plotted density of states shown in figure 8.1. We only include the DOS of this particular super-cell because results of the most stable arrangement is probably the most representative of a potential high-entropy silicide, nevertheless we will consider the remaining SQSs in the following sections as well.

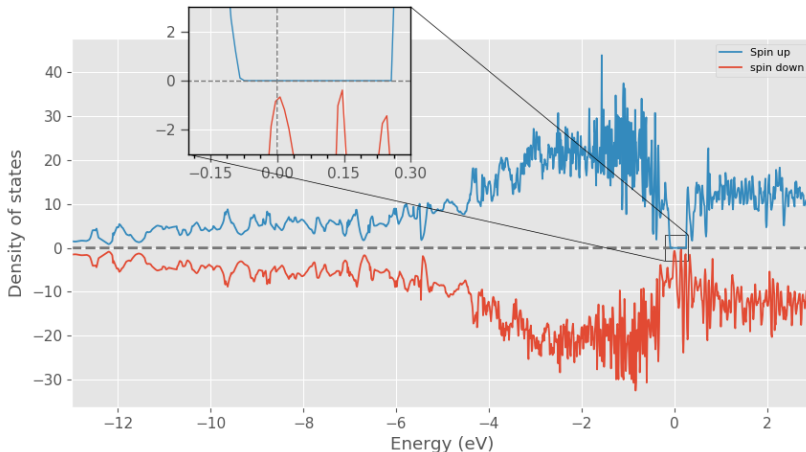


Figure 7.1: Density of states SQS D CFMN (fesi2) from PBE calculation

From the DOS we observe that the band gap in this structure differ between the spin up states and spin down states, following the magnetic property of the material seen in table 8.1. In this particular SQS the spin down channel is completely metallic, and the spin up channel exhibit a relatively large band gap, thus we can classify this SQS as either a half-metal, or possibly a spin-gapless conductor (**Insert references/discuss this**). Furthermore we find that the band gap in all SQSs of this alloy is severely spin-polarized in the spin up direction **Is this okay to say?**. We list the spin-dependent band gaps in table 8.3, and show the relationship in SQS B in figure 8.2 bellow.

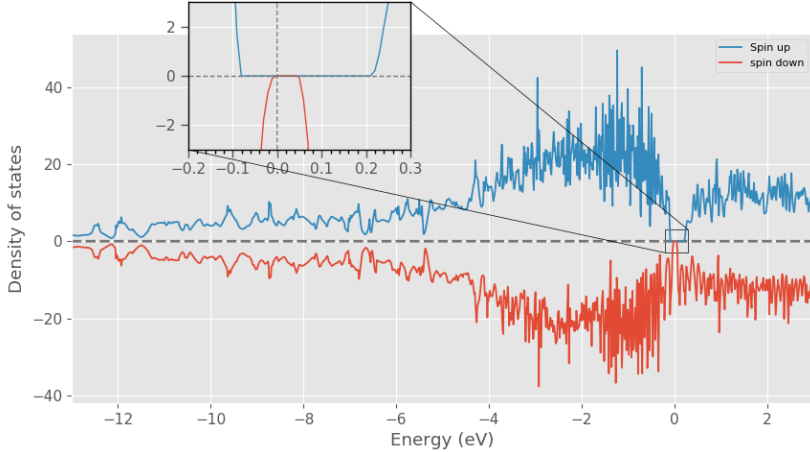


Figure 7.2: Density of states SQS B CFMN (fesi2) from PBE calculation

Structure	Spin-up	Spin-down	Total
A	0.0814	0.0522	0.0281
B	0.2932	0.0523	0.0523
C	0.2355	0.0343	0.0343
D	0.3386	0	0
E	0.3078	0.0495	0.0495

Table 7.3: Band gap (eV) with PBE in spin up and spin down channels of CFMN (fesi2) SQSs

From table 8.3 we find that SQSs B, D and E all display band gaps around 0.3 eV in spin up, and small non-zero or zero band gap in the case of SQS D in spin down. In the coming section we will investigate the band gap and electronic structure of this compound by looking at the local and projected density of states.

7.1.3 Local and Projected density of states

From LDOS and PDOS it's possible to study the above case by the contributions of the individual elements in the structure. In the local density of states plotted in figures 8.3 and 8.4 we see that the s-electrons in Si occupy states in the lower energy regions and the p electrons at energies closer to the Fermi energy, while both equally occupy states above E_F . In the transition metals we see that 3d electrons dominate across the energy range. Between the different TMs we observe that 3d electrons particularly of manganese and chromium show a strong presence in spin down right above E_F , and just below in the spin up direction. Meanwhile iron and nickel lie at lower energies respectively. The relationship and interaction between the different elements can better be seen in the projected density of states in figure 8.5.

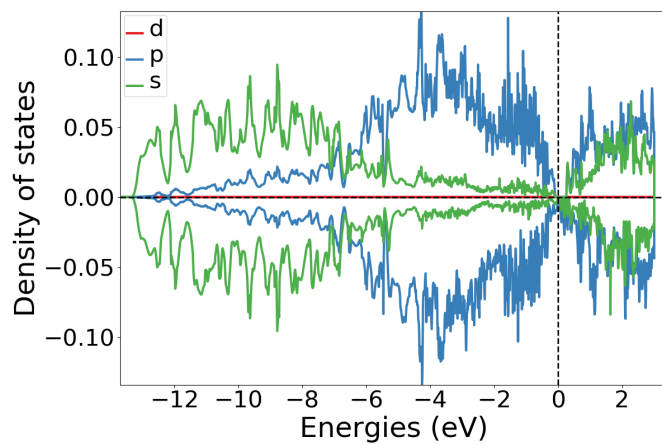


Figure 7.3: Local density of states of Si (SQS D)

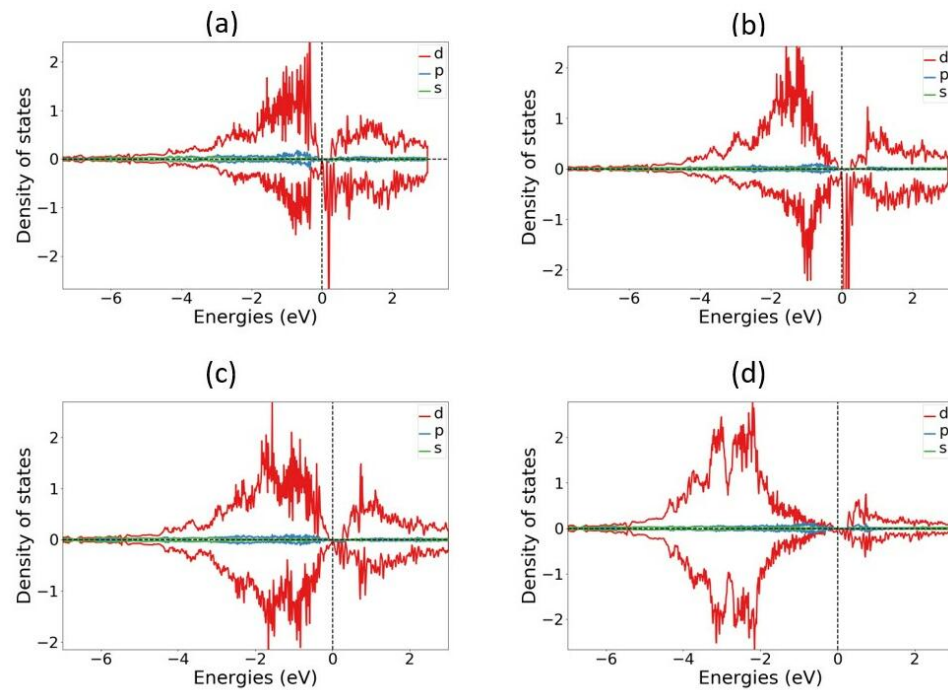


Figure 7.4: Local density of states of TMs (SQS D), (a) Cr, (b) Mn, (c) Fe, (d) Ni

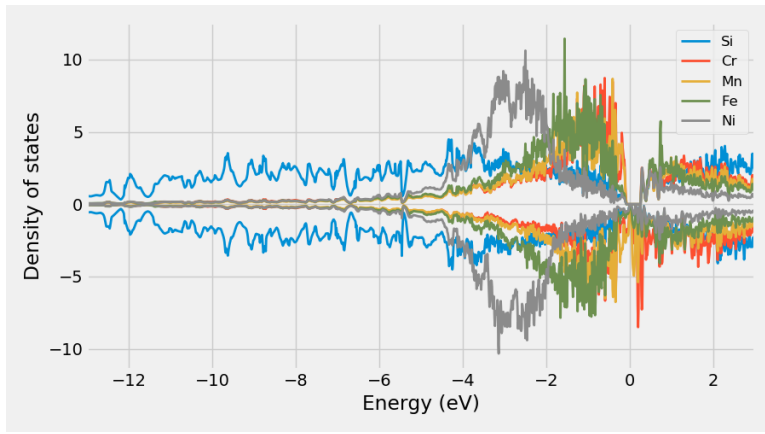


Figure 7.5: Projected density of states SQS D CFMN (fesi2) from PBE calculation

In agreement with the local DOS we observe here that the Si s-electrons occupy the lower energetic states, and evidence of p-3d hybridization at higher energies. With the upmost energetic states in the valence band occupied by 3d electrons of chromium and manganese. Below we include the PDOS of SQS D and B but focused around E_F , from these figures we find that the spin down channel in D contain a more dominant presence of manganese especially, and some chromium as compared to the semiconducting SQS B.

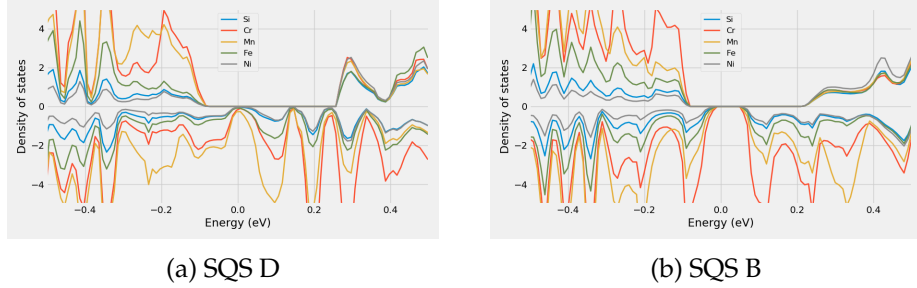


Figure 7.6: Projected density of states of SQS D and B around E_F

In the context of DFT and VASP there are several factors than can affect the accuracy of the DOS. As mentioned in section .., the type of numerical smearing is paramount for accurate DOS calculations. In this project we experienced large differences between calculations from gaussian and TBC smearing in relation to the band gap and DOS, this will be covered in more detail later. Moreover the DOS is very sensitive to computational factors such as the number of points (NEDOS in VASP) and the number of k-points (to solve the DOS integral, see section ..). For example, the band gap in structure C could only be seen in the density of states when increasing the number of points in the DOS from 2401 to 20000 points. This is shown below in figure .., where we plot the density of states around the fermi energy, denoted by the stippled red and blue lines, relative to the density of states with 2401 points and 20000 points respectively, all

other parameters remained unchanged. It should however be noted that the second calculations applied the charge density calculated by the former for quicker convergence.

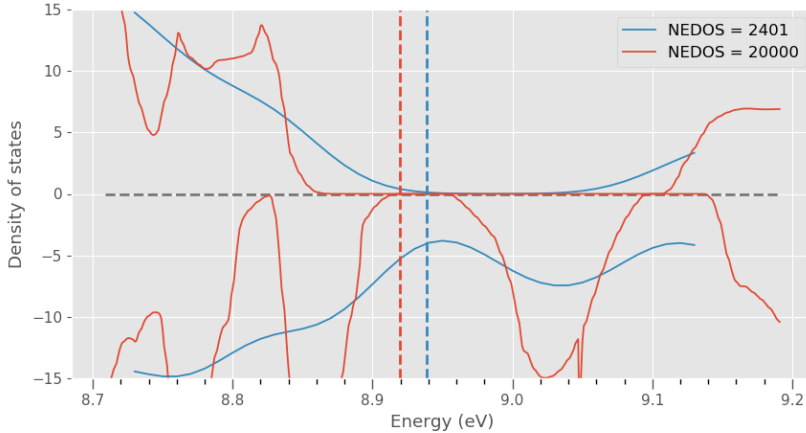


Figure 7.7: Density of states of SQS C with 2501 points vs 20000 points in the density of states.

Despite of the higher accuracy of the greater number of points, we continue to perform calculations with around 2400 points, mostly down to the increased workload of analyzing the DOS with such a large number of points.

Some way of visualizing the eigenvalues? To explain the result of SQS D in comparison to the other semiconducting SQSs of the alloy, we look at the calculated eigenvalues for the distinct supercell. Here it's seen that eigenstates transition between full to empty occupancy at energy band 124 in spin down and 129 in spin up, thus a difference of 5 bands between states in the different spins, this is also the case in the other SQSs. In particular of SQS D however is that for a majority of k-points the bands 124 and 125 contain occupancy values other than 1 and 0 for the spin down states. These are either non-physical values above 1 or negative, in other words indicating states are more than filled or less than empty. Or values in-between 1 and 0, meaning partially filled states (defect states). If we were to neglect these defect states and only consider bands where the occupancy is above 0.99 or bellow 0.01, the band gap of structure D remain consistent in spin up, but we now observe a band gap of around 0.05 eV in the spin down channel as well. Again, this would have been extremely insightful to investigate with the help of a band structure diagram. The non-physical values is simply a consequence of using the tetrahedron method with Bloch corrections (ISMEAR-5) as numerical smearing, ([Insert reference](#)). Interestingly we only find such values for spin channels also containing defect states. Furthermore the presence of such defect/non-physical states is found as the key divider between structures with and without a band gap also for the coming examples in this project.

7.1.4 Meta-GGA and hybrid functional

As expressed previously, in this work we invoke 3 level of depths GGA (PBE), meta-GGA (SCAN) and hybrid functionals (HSE06) to determine the band gap of the SQSs. In table .. bellow we list the respective band gaps of these methods for all 5 SQSs of CFMN (fesi2). Note that all calculations is done with TBC smearing.

Structure	PBE	SCAN	HSE06
A	0.0281	0.0000	0.0207
B	0.0523	0.0890	0.1808
C	0.0344	0.0690	0.0196
D	0.0000	0.0000	0.0000
E	0.0495	0.1048	0.0133

Table 7.4: Band gap of CFMN (FeSi_2) SQSs with GGA (PBE), meta-GGA (SCAN) and hybrid-functionals (HSE06).

The most obvious result of table .. is that aside from SQS A, all 3 methods agree on the presence of the band gap. This in itself is a very positive result for this project, as the primary motivation is based simply on locating semiconducting high-entropy silicides and thus the agreement of 3 different methods on the same structures is most welcome. On the other hand, it's clear that the actual size of the gap is under some debate. We note the largest observed band gaps is largely associated with the SCAN functional, compared to PBE calculations this result is very in line with what is expected by involving more complex factors in the calculations, as discussed in section .. In contrast, by the same argument we would not expect that par SQS B, the overall smallest band gaps is found with the well-proven hybrid functional HSE06, as shown in table .. The results associated with the HSE06 functional will be covered in more detail in the subsequent section, for now lets consider SCAN.

SCAN

On the surface the results with SCAN are sensible and in line with the PBE results with the exception of SQS A, in this case the calculations with SCAN resulted in a zero band gap as opposed to 0.03 eV with the PBE functional. However also the SCAN results of the other 4 SQSs differ from the PBE band gaps. In the two SQSs B and E the band gap is increased with SCAN, but the properties of the gap is reversed compared to PBE. This is shown in figure 8.8 for SQS E. The band gap of this SQS as previously described is around 0.3 eV in spin up and 0.05 eV in spin down equaling a total 0.05 eV band gap. Bellow in figure 8.8 it's seen that the SCAN functional results in a larger total gap of 0.09 eV, but at the same time lowers the previously large spin up gap, and increase the smaller spin down gap. This is also seen in SQS B. In structures C and D this is taken a step further and reverse the spin polarization of the band gap. **Include**

figure?. For example, in despite of the SCAN functionals agreement with PBE of predicting a zero total band gap in SQS D, the former in opposite of PBE find a band gap in the spin down channel.

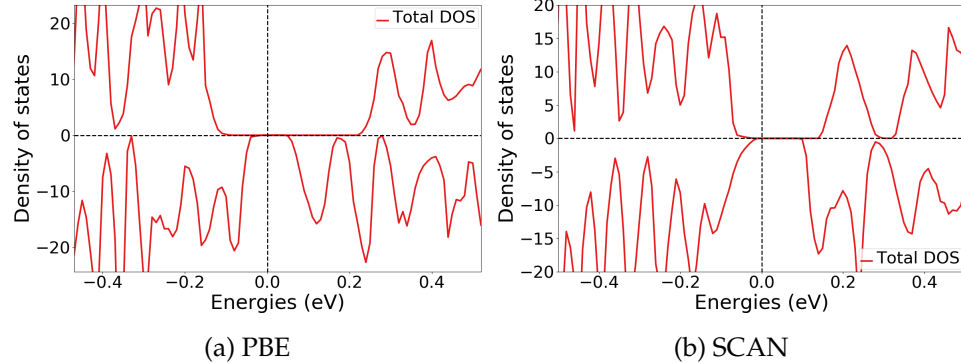


Figure 7.8: Density of states of SQS E illustrating the different band gap from calculations with (a) PBE and (b) SCAN functional

HSE06

As stated above, the measured band gaps with the HSE06 functional was less than that of PBE and SCAN for most of the tested SQSs. Hybrid functionals as described in section .. is computationally demanding, but comes with superior accuracy for band gap measurements, and the HSE06 functional in particular is on the top of the list. For this reason, one would in general expect larger band gaps compared to GGA or meta-GGA calculations, as highlighted in .. cite? The one exception we observed to this trend is in SQS B (figure 8.9 A), here the band gap increase from 0.05 eV to 0.09 eV and 0.18 eV from PBE to SCAN to HSE06. One possible reason behind the abnormally large gap can originate from the small number of k-points we had to employ in order for the calculations to converge. Recalling that the gap transition in in the PBE calculation was (0.250,0.000,0.250)-(0.000,0.000,0.000), compared to the hybrid functional we now see that the transition is between k-points (0.500,0.000,0.000) and (0.000,0.000,0.000). Moreover, the point (0.250, 0.000, 0.250) in k-space is not included in the hybrid functional due to the narrow mesh (this we read from the IBZKIT file in VASP). Thus it's a possibility that the large gap is caused by the fact that the minimal gap is not encapsulated by the k-points in the HSE06 calculation. However we also see this trend in the other SQSs, but despite of the different transistion in k-space, these structures find lesser band gaps with the HSE06 functional compared to PBE. Additionally, we find similar results in the bulk β -FeSi₂ structure. In this calculation we applied the same number of k-points for HSE06 as for PBE and SCAN. Nevertheless we find a much larger band gap of around 1.5 eV with HSE06, as opposed to 0.65 eV with both PBE and SCAN, and as mentioned before the two latter is in much better agreement with experimental results and ab intio work on the band gap of β -FeSi₂ cite materials project, other articles. Additionally also in this case, the transition vary between functionals.

PBE: (0.000,0.000,0.000)-(0.000,0.000,0.250), and HSE06: (0.000,0.000,0.000)-(0.000,0.000,0.500). **Include band-diagram for bulk fesi2?**

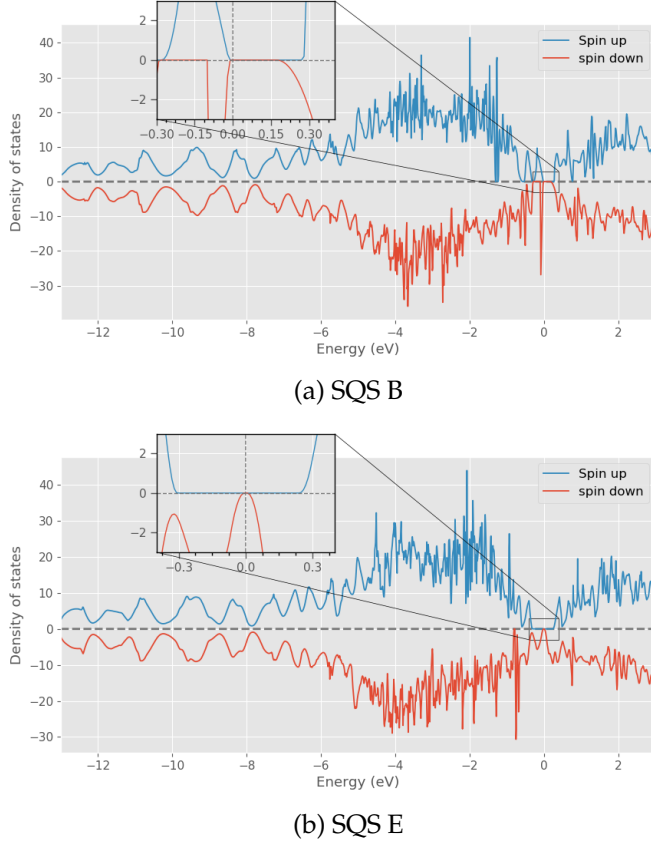


Figure 7.9: Total density of states of SQS (a) B and (b) E from calculations with HSE06

Aside SQS B, we generally see good agreement between HSE06 and PBE calculations. In A we notice that the 0.02 eV band gap stems from a 0.7 eV gap in spin up and 0.02 eV in down. Likewise SQSs C, D, and E all exhibit large band gaps in spin up, 0.17, 0.37 and 0.55 eV respectively, and correspondingly very narrow spin down gaps 0.032, 0, and 0.013 eV. In figure 8.9 above we include the plotted density of states for SQS B (a) and E (b) clearly illustrating the spin polarization in E. Compared to the listed spin dependent band gaps from PBE in table 8.3, we see that the band gaps from HSE06 typically compares or exceeds in spin up, and lessen in spin down, with the exception of SQS B (0.29 eV and 0.18 eV) where also the spin down gap is increased.

Numerical smearing

Rewrite/reconsider this paragraph, is it needed? How can I write this more concise? Figure? One final point we would like to cover in the discussion of HSE06 calculations of this system, and generally in this project, is the effect of smearing on the reported band gaps. From the

method section, we know that TBC smearing is the preferred choice for accurate density of states and total energy calculations of semiconductors, alike we know that this method is unfitting to calculate the forces in metals. As discussed in the methodology section, hybrid functionals proved difficult to converge for such compositionally complex structures, thus we were forced to initially calculate the charge density from the HSE06 functional with did a self-consistent calculation with gaussian smearing and smearing width of 0.05 eV. Thereafter reuse the calculated charge density for subsequent hybrid calculations with TBC smearing. Using SQS A as an example, from the first run (Gaussian), the band gap is 0.15 eV, (0.78 up and 0.15 down). However the eigenvalues contain defect states and the band gap is not observable from the density of states. Next we can reapply the charge density to perform an additional HSE06 calculation with gaussian smearing, but reducing the smearing width from 0.05 eV to 0.005 eV. Now we find a new gap of 0.1 eV (0.21 up and 0.1 down), with no defects in the eigenstates, and apperant in the density of states. In cases where we find conflicting results between the eigenvalues and density of states we rely on the script bandgap.py provided in the pymatgen package, refer to section .. for a description. With this we only report a band gap for the HSE06 calculation with TBC smearing, note that this method return the same value of the gap as well. As another example lets consider SQS B. In contrast, the numerical smearing does not appear to impact the band gap of this structure. We find from HSE06 simulations with gaussian smearing of both 0.05 and 0.005 eV smearing width to yield results around 0.28 eV and 0.18 eV in spin up and down. But alike SQS A, the larger smearing width comes with a few defect states in the spin down channel and additionally can not be seen in the density of states. However, particular of this structure is that the bandgap.py script validate the calculated total band gap from the eigenvalues in all three calculations. Aside from this abnormalty, the other SQS similar to A find some similarities between smearings, but only TBC was validated with bandgap.py, furthermore the DOS does not with the same clarity reproduce the calculated band gap from the eigenvalues in calculations done with gaussian smearing compared to TBC. **figureof the DOS of hybrid/smear/smear5 maybe A?**

We see from the above examples that as most studies and articles state, that TBC smearing is superior in terms of accurate total energy and DOS calculations of semiconductors. Similar to how TBC produce inaccurate forces of metals, in several cases in this project we relaxed the structures with gaussian to forces bellow 1E-2, but subsequent calculation with TBC in certain cases resulted in forces above 0.1, without making any geometric alteration to the previously relaxed cell (**Include examples?**). On the grounds of these factors we can report good agreement between our own results and the theoretical advice regarding numerical smearing in DFT studies **Insert references**

Figure on cpu time pbe vs scan vs hse06.

Fro the above examples between it's clear that the band gap in this compound is subject to the SQS and the applied exchange-correlation functional. From the SCAN functional we found several cases that

disagreed with the PBE results, see SQS A, C and D. Combining this with the popularity and wide-spread application and reliability of the PBE functional. See for example materials project, that exclusivly list PBE band gaps, and other relevant studies **refrences**. We put the most faith in the PBE results. An additional point is that GGA is known to underestimate band gaps, due to the concepts described in section .., therefore if we find a gap with PBE, the real material would most probably also have a band gap, and a larger one at that.

Regarding the HSE06 functional, the inaccuracy shown for the bulk material is concering, escpecially considering the lack of experimental baselines in this study to compare and measure our results after. However, generally we find much better cohesion between PBE and HSE06 compared to SCAN for the 5 supercells, both methods predict semiconductors with heavy spin polarization in the spin up direction, par B. The fact that all 3 functionals and five structures for the most part agree on the presence of a semiconductor is a overwhelmingly positive result in itself, that allow us to state with high certainty that this compound is in fact a semiconductor, or we may label the compound as a half-metal or spin-gapless conductor from the registered spin dependence. A qualitative study on the exact band gap would demand a much greater scope as there are many factors affecting the value that we have neglected. One of these is the randomness involved with SQSs. For instance, by increasing the SQS size, ie number of atoms in the supercell, we found again different band gaps, but still, the presence and character of the compound was consistent. **Include this? Table?** To draw any meaningfull conclusions on the size of the band gap would requiere us to both increase the number of SQS's of the composistion due to the obseved variation in the band gap between the 5 tested supercells, and as well for different supercell sizes to obtain some sort of convergence of the band gap. On the other hand, if we were to go by the most stable configuration of this narrow study, then this alloy would be labeled as a half-metal from the results of SQS D across all three functionals.

7.1.5 Probability distribution functions and charge density

In this final segment of the CFMN alloys we will look at the probability distribution functions and charge density. We only include the results of SQS B and D as an in-depth across 5 unieq structures become tedious and time-consuming, the PDFs of the remaining structures can be seen in appendix ..

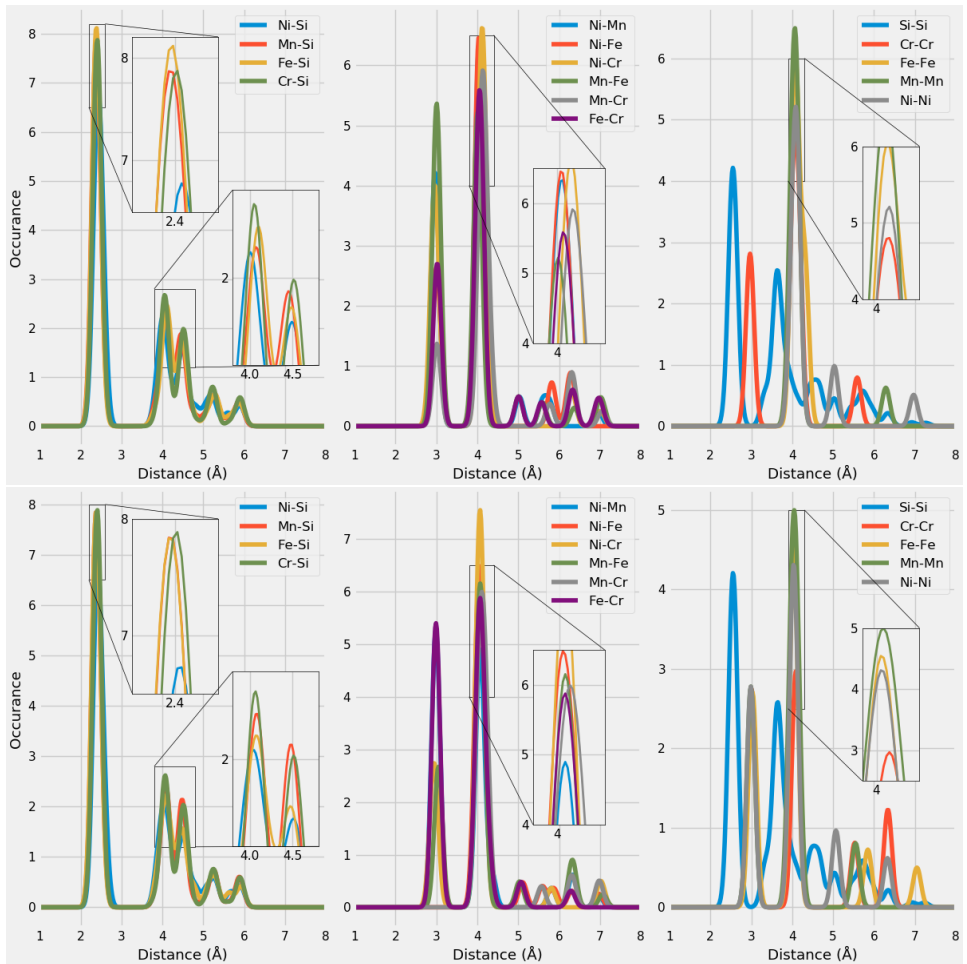


Figure 7.10: Probability distribution function of SQS D (top) and B (bottom)

We see that the relative positions of the PDFs remain consistent though both SQSs. With the aid of the ICSD (insert citation), we can compare the figure .. to the expected PDFs based on a number of experiments from a host of different compounds. As our compound contain a total of 15 different bonds, comparing each one to the ICSD values would be an exhaustive process. For our purpose we are satisfied by comparing the 4 different metal-Si bonds. We find that the preferred bond-length of TM-Si is observed at two values, the most dominant being the shorter of the two. For Fe-Si these are between 2.25-2.75 and 4-5, Mn-Si 2.25-2.75 and 3.5-5. Ni-Si lie between 2.25-2.5 and 3.85-5 and Cr-Si between 2.35-2.65 and 4-5. Clearly, the PDFs of the alloys are in good agreement with the listed values for Tm-Si bonds, with the most occurring bond length falling at around 2.4 Å for all TMs, and lesser occurrence between 4.0 - 4.5 Å. The height of the respective peaks is somewhat consistent in both structures, other than slightly reduced Fe-Si occurrence at 2.4 Å in B.

In contrast to the TM-Si bonds, we observe several distinctions between metal bonds in SQS D and B. Covering all would be tedious and not too insightful, instead we emphasize the bonds of Mn and Cr as this is where

we found the biggest discrepancy in the PDOS. From the different TM-TM bonds (middle) of figure 8.8 we observe that the Mn-Fe bonds are most occurring at short distances in D and bigger distances in B, meaning that manganese and iron atoms are placed further from each other in structure D. **correct?** Similarly the bonds between Cr and Fe indicate that these atoms lie closer in B than D. In contrast the nickel and manganese/chromium bonds point to a closer distance in B for Ni-Mn and Ni-Cr in D, and a greater distance between Ni and Mn in D and Ni and Cr in B. **Litt kronglete kanskje?** In terms of the homogeneous bonds, the properties of both Cr-Cr bonds and Mn-Mn bonds are more or less alike in both structures besides some majority at shorter distance in D (The red Cr-Cr line at 3 Å is underneath the grey Ni-Ni line in B in figure 8.8 (bottom right)). A more significant distinction is that both Ni-Ni and Fe-Fe bonds are found at 3 Å and 4 Å in B, but exclusively 4 Å in D.

Both the Fe-Fe and Ni-Ni bonds are in better agreement with the ICSD histograms, as the most occurring distance for these bonds are between 4-4.9 Å and additionally around 2.5 Å. **More comparisons to ICSD, ask O.M.** As a conclusion on the PDFs of this compound, we locate a pattern where the Si-Si bonds are identical and only very minor differences between TM-Si bonds in SQS D and B. This is a result of how the structures are generated with the SQS method. In the FeSi₂ structure the silicon atoms are placed as before in the new supercells, but the TM elements are "randomly" distributed. Thus, it's reasonable that also here we would find the major differences between SQSs in the PDFs.

Bellow we show the calculated charge density (from PBE) of structure B (left) and D (rights) **What should I say about these?**

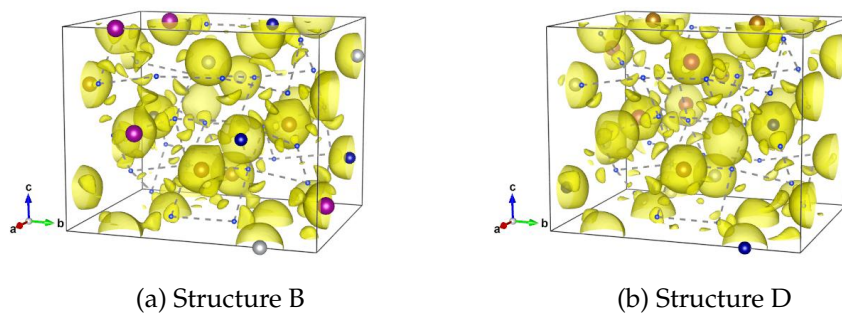


Figure 7.11: Charge density of SQS D and B from PBE calculations. Illustrated by VESTA

7.2 Permutations of the Cr₄Fe₄Mn₄Ni₄Si₃₂ high-entropy silicide

Up until this point we have looked in detail at the high-entropy silicide (CrFeMnNi)Si₂ and associated SQSs. However these structures are just the center of a larger quasi-ternary phase diagram consisting of the

different possible distributions of elements. Thus there exists many more permutations of this particular composition of a high-entropy silicide. In this section, we aim to expand our search of this diagram by generating SQSs slightly away from eqvimolar distribution of 3d elements. In table (bellow) we list the mean total energy and magnetic moment per atom with standard deviation and the enthalpy of formation of 4 permutations of the $(\text{CrFeMnNi})\text{Si}_2$ alloy. Ideally the permutations would differ only by one element, but the TDEP implementation insist in also reducing Nickel to stay consistent with the 48 atom supercell.

	Total energy/atom (eV)	Enthalpy of formation (eV)	Final magnetic moment (μ_B)
$\text{Cr}_3\text{Fe}_3\text{Mn}_7\text{Ni}_3\text{Si}_{32}$	- 6.6947	0.0040	-11.9586
$\text{Cr}_5\text{Fe}_5\text{Mn}_3\text{Ni}_3\text{Si}_{32}$	- 6.6705	0.0030	-11.1991
$\text{Cr}_5\text{Fe}_3\text{Mn}_5\text{Ni}_3\text{Si}_{32}$	- 6.6852	0.0041	-10.5200
$\text{Cr}_3\text{Fe}_5\text{Mn}_5\text{Ni}_3\text{Si}_{32}$	- 6.6801	0.0036	-12.6426
$\text{Cr}_3\text{Fe}_3\text{Mn}_3\text{Ni}_7\text{Si}_{32}$	- 6.3921	0.0078	-10.9614

Table 7.5: Mean and standard deviation of the total energy and magnetic moment per atom, plus enthalpy of formation of the listed mean energies (FeSi_2).

The first result of table .. we make notice of is that the stability, as evaluated by the enthalpy of formation can be increased beyond the eqvimolar composition. This is accomplished in two distinct permutations, one with increments to manganese relative to the other TM, and the other by reduction of chromium. Moreover the two respective permutations lie on the opposite side of the magnetic scale. The large magnetic moment of the manganese rich permutation and the low magnetic moment in the chromium poor permutation is very much in line with the observations made in the previous section. Recalling that in the magnetic moment in the eqvimolar composition was largely attributed to manganese and chromium atoms in the lattice. Thus increments to manganese or reduction of chromium would following impact the magnetic moment as in the two permutations. For this reason, additionally the permutation $\text{Cr}_5\text{Fe}_3\text{Mn}_5\text{Ni}_3\text{Si}_{32}$ where the nonmagnetic elements is reduced and the magnetic elements are increased ,is equally magnetic. We however find no direct relation between stability and magnetism as his particular permutation is the least stable. An important property of table 8.5 is that the listed values are the mean value of the observed property for 5 distinct SQSs of the same permutation. For example we notice that while the highest magnetic moment in the first permutation is associated with the most stable SQS (from total energy considerations). The least stable supercell show the highest magnetic moment in $\text{Cr}_5\text{Fe}_3\text{Mn}_5\text{Ni}_3\text{Si}_{32}$.

The respective band gap of the permutations (with PBE) can be seen in table ... Compared to the previous case, we find most SQSs of the permutations to exhibit a half-metallic character.

		Spin up (eV)	Spin down (eV)	Total (eV)
$\text{Cr}_3\text{Fe}_3\text{Mn}_7\text{Ni}_3\text{Si}_{32}$	A	0.3390	0	0
	B	0.4745	0	0
	C	0.1342	0	0
	D	0.1950	0.0063	0.0063
	E	0.4211	0	0
$\text{Cr}_5\text{Fe}_5\text{Mn}_3\text{Ni}_3\text{Si}_{32}$	D	0.0674	0.0413	0.0372
$\text{Cr}_5\text{Fe}_3\text{Mn}_5\text{Ni}_3\text{Si}_{32}$	A	0.2082	0	0
	B	0.4053	0	0
	C	0.4659	0	0
	D	0.0843	0.0121	0.0121
	E	0.3008	0	0
$\text{Cr}_3\text{Fe}_5\text{Mn}_5\text{Ni}_3\text{Si}_{32}$	A	0.3922	0	0
	C	0.1285	0	0
	D	0.2595	0.1004	1.004
	E	0.3591	0.1003	0.0848
$\text{Cr}_3\text{Fe}_3\text{Mn}_3\text{Ni}_7\text{Si}_{32}$	-	-	-	-

Table 7.6: Total and spin dependent band gap of 4 permutations of CFMN (fesi2) with PBE GGA calculation. The structures that are excluded from this list either failed in calculations, or does not show any band gap.<

From table .. we see that likewise to the stability and magnetization also the band gap changes in the different directions. To some degree we find positive results of the band gap in each direction, but we see particularly that permutations rich in manganese provide very encouraging results. This is made clear from the fact that $\text{Cr}_3\text{Fe}_3\text{Mn}_7\text{Ni}_3\text{Si}_{32}$, $\text{Cr}_5\text{Fe}_3\text{Mn}_5\text{Ni}_3\text{Si}_{32}$ and $\text{Cr}_3\text{Fe}_5\text{Mn}_5\text{Ni}_3\text{Si}_{32}$ all include amounts of manganese higher than the eqvimolar composition and all associated SQSs show at least strong half-metallic character or semiconducting. On the other side $\text{Cr}_3\text{Fe}_3\text{Mn}_3\text{Ni}_7\text{Si}_{32}$ is the sole permutation with less manganese and correspondingly show the least sign of a band gap. Moreover the relative stability of the SQSs give further merit to the proposition. In the first permutation we find that the highest total energy is associated with SQS B, which as seen in table .. exhibit the largest spin up band gap of the particular permutation. Furthermore the two semiconducting SQSs in the last permutation is the two most stable arrangements. Reversely, in the manganese-poor permutation we find that the sole semiconducting SQS is the second least stable of that compound. Lastly, the opposite is the case is true in the third permutation. Despite the total energy not varying tremendously between SQSs of the same permutation, as seen by the standard deviation in table .., the continuing trend between stability and band gap is a promising result to report.

In figure 8.12 we plot the projected density of states around E_F of the 4 permutations. Note that away from the Fermi energy the projected density

of states is analogous to the parent compound, see appendix ..

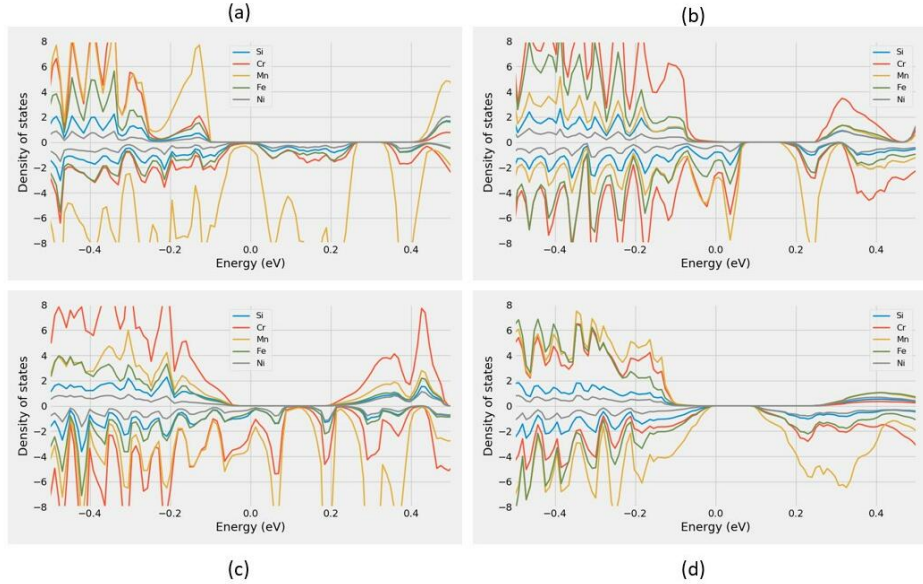


Figure 7.12: Projected density of states of (a) $\text{Cr}_3\text{Fe}_3\text{Mn}_7\text{Ni}_3\text{Si}_{32}$ (SQS B), (b) $\text{Cr}_5\text{Fe}_5\text{Mn}_3\text{Ni}_3\text{Si}_{32}$ (SQS C), (c) $\text{Cr}_5\text{Fe}_3\text{Mn}_5\text{Ni}_3\text{Si}_{32}$ (SQS A), (d) $\text{Cr}_3\text{Fe}_5\text{Mn}_5\text{Ni}_3\text{Si}_{32}$ (SQS D)

The above figures is based on the most stable SQS in each permutation, as will the analysis. Thus the features of these figures does not necessarily represent the complete set of SQSs of the permutation. As experienced in table 8.6 and previous examples in this project, the band gap and properties of each permutation can vary between SQSs. But given that the structures came out on top in terms of total energy means that they are the most probable configuration of the real alloy, hence also the features of that supercell.

With that said, the plotted PDOSs in figure 8.12 clearly illustrate the characteristics shown in table 8.6. We see clear indication of a spin up band gap in $\text{Cr}_3\text{Fe}_3\text{Mn}_7\text{Ni}_3\text{Si}_{32}$ (a) and $\text{Cr}_5\text{Fe}_3\text{Mn}_5\text{Ni}_3\text{Si}_{32}$ (c), and a total band gap in $\text{Cr}_3\text{Fe}_5\text{Mn}_5\text{Ni}_3\text{Si}_{32}$ (d). Not so clear is that the density of states of $\text{Cr}_5\text{Fe}_5\text{Mn}_3\text{Ni}_3\text{Si}_{32}$ (b) contain very small nonzero values at E_F and the unoccupied states is shifted very slightly above the Fermi energy, prohibiting an otherwise clear band gap. In figure 8.13 the total density of states of SQS D and E of this permutation is shown, the above point is seen also in SQS E, where the "band gap" is shifted above E_F .

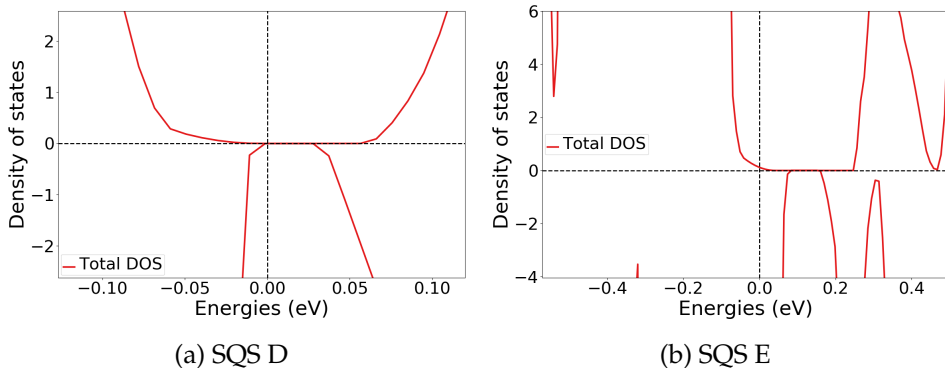


Figure 7.13: Density of states around E_F of SQS D and E $\text{Cr}_5\text{Fe}_5\text{Mn}_3\text{Ni}_3\text{Si}_{32}$

In figure 8.6 we saw that electrons from manganese atoms in particular was a key contributor as to why the spin down channel of $(\text{CrFeMnNi})\text{Si}_2$ was metallic in the stable supercell D. This is also largely the case in the permutations shown above in figure 8.12.

The proportion of manganese atoms in the alloy seems to offer a very positive effect on the band gap in spin up, but is often detrimental to spin down. This is seen in figure 8.12 (a) and (c) for $\text{Cr}_3\text{Fe}_3\text{Mn}_7\text{Ni}_3\text{Si}_{32}$ and $\text{Cr}_5\text{Fe}_3\text{Mn}_5\text{Ni}_3\text{Si}_{32}$ respectively, that both contain increased amounts of manganese. By reducing the number of Mn as in (b) we still find that the Mn electrons plague the states at E_F in spin down. In analog we see from (b) and (c) that also Cr negatively impacts to the band gap especially in spin up. The sole permutation with clear evidence of a spin down gap is from the chromium poor permutation plotted in (d). Also in this structure we see that the effects of Mn around E_F is dampened in comparison to the other permutations, despite containing relatively increased amounts of Mn to the eqvimolar alloy.

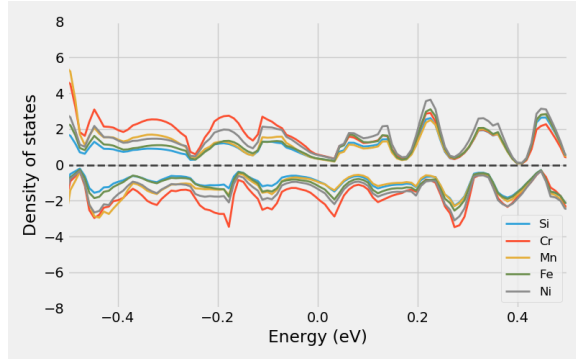


Figure 7.14: Projected density of states of $\text{Cr}_3\text{Fe}_3\text{Mn}_3\text{Ni}_7\text{Si}_{32}$ around E_F

An important property of these results is that because each permutation alters simultaneous elements, interpreting and relating the results to a particular alteration is challenging. For example, is the result of the $\text{Cr}_5\text{Fe}_3\text{Mn}_5\text{Ni}_3\text{Si}_{32}$ permutation a consequence of less Fe or increments to both Cr and Mn? Furthermore is the exaggerated band gap in spin

up of $\text{Cr}_3\text{Fe}_3\text{Mn}_7\text{Ni}_3\text{Si}_{32}$ a product of increasing manganese or reducing the other elements. From the comparatively large gaps in spin up of $\text{Cr}_3\text{Fe}_3\text{Mn}_7\text{Ni}_3\text{Si}_{32}$ and $\text{Cr}_3\text{Fe}_5\text{Mn}_5\text{Ni}_3\text{Si}_{32}$ and the more present Cr states in spin up in the Cr rich permutations we here conclude that the band gap is related to lessening of chromium, more so than other effects. Despite of this we generally find positive results regarding most of the permutations as seen in table 8.6, the exception to this $\text{Cr}_3\text{Fe}_3\text{Mn}_3\text{Ni}_3\text{Si}_{32}$. This particular permutation in opposition to the others in this section increases the proportion of Ni at the cost of the other 3d elements. The projected density of states is displayed in figure [REF]. From both this structure, but also the PDOS of $\text{Cr}_3\text{Fe}_3\text{Mn}_7\text{Ni}_3\text{Si}_{32}$ we see that reducing chromium does not always improve the band gap. It's clear that the $\text{Cr}_3\text{Fe}_5\text{Mn}_5\text{Ni}_3\text{Si}_{32}$ alloy manage to strike a balance of distribution that results in a specific interplay between the 3d elements. For this reason we more closely investigate the properties of this structure, the probability distribution of SQS D (highest stability) is plotted bellow in figure 8.15.

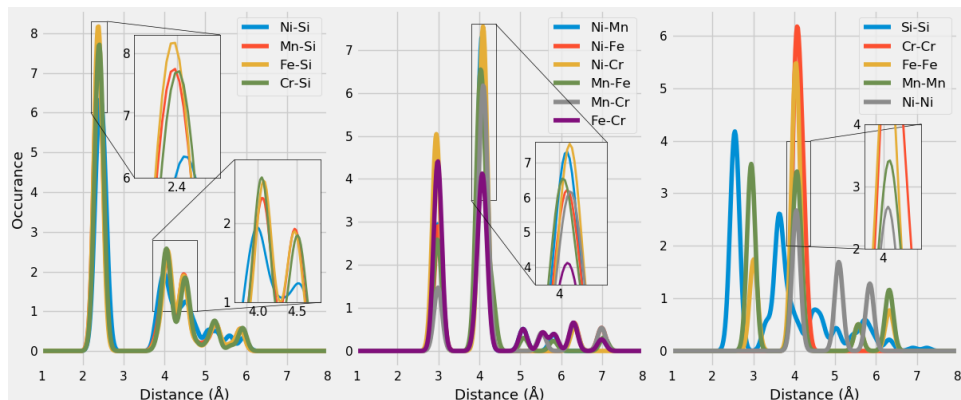


Figure 7.15: Probability distribution functions to $\text{Cr}_3\text{Fe}_5\text{Mn}_5\text{Ni}_3\text{Si}_{32}$ SQS D, Maybe make larger

Comment figure

Add some figures from HSE06? In this segment of the project we scarcely applied the more advanced functionals SCAN and HSE06, in part to both the uncertainties mentioned in the previous section and the computational cost of the methods. However we did perform such calculations (HSE06) to further investigate the nature of the listed semiconducting SQSs. Both the manganese rich and poor semiconductors are validated with the HSE06 functional and find wider band gaps of 0.17 eV (0.57 and 0.26 in up and down) in $\text{Cr}_3\text{Fe}_3\text{Mn}_7\text{Ni}_3\text{Si}_{32}$ SQS D, and 0.22 eV (0.77 eV in spin up) in $\text{Cr}_5\text{Fe}_3\text{Mn}_3\text{Ni}_3\text{Si}_{32}$ SQS D. On the opposite side, the very narrow band gap in $\text{Cr}_5\text{Fe}_3\text{Mn}_5\text{Ni}_3\text{Si}_{32}$ vanishes with HSE06 calculations. For the two stable semiconductors found in $\text{Cr}_3\text{Fe}_5\text{Mn}_5\text{Ni}_3\text{Si}_{32}$, simulations with the HSE06 functional resulted in a half-metal with a spin up of 0.53 eV for SQS D, and a total band-gap of 0.27 eV for E, where the spin-up gap is 0.73 eV wide. Comparing to table 8.6 we observe that ...

**As for the SCAN functional ...
Conclusion this section**

Chapter 8

Changing the elements

In similar fashion to the previous sections, we here begin by presenting the mean and standard deviation of the total energy and magnetization of a set of SQSs corresponding to different high-entropy silicides of the FeSi_2 unit cell. The compositions we have tested are deliberate combinations intended to investigate both the impact of manganese by replacing the element with Co or Ti, and concepts related to HEA theory such as the atomic size effect. Furthermore Co is a very common element in many stable HEA, as seen in section .., thus we include two (3?) compositions with this element to study the impact on stability and the functional properties. The results of the aforementioned alloys can be seen bellow in table 9.1, note that all compounds contain a total of 48 atoms as before.

	Toten (eV)	Enthalpy of formation		Mag	
$\text{Cr}_4\text{Fe}_4\text{Co}_4\text{Ni}_4\text{Si}_{32}$	- 6.4655	0.0056	- 12.7536	0.0083	0.0155
$\text{Co}_4\text{Fe}_4\text{Mn}_4\text{Ni}_4\text{Si}_{32}$	- 6.4731	0.0046	- 15.0836	0.0000	0.0000
$\text{Cr}_4\text{Fe}_4\text{Ti}_4\text{Ni}_4\text{Si}_{32}$	- 6.4217	0.0087	- 7.5040	0.0305	0.0293
$\text{Cr}_4\text{Fe}_4\text{Mn}_4\text{Ti}_4\text{Si}_{32}$	-6.6994	0.0071	- 7.3060	0.1142	0.0641
$\text{Cr}_4\text{Fe}_4\text{Mn}_4\text{Co}_4\text{Si}_{32}$	-6.7687	0.0034	- 13.7796	0.1331	0.0326

Table 8.1: Summary of the total energy, enthalpy of formation and magnetization of several compositionally different SQS high-entropy alloys based on the $\beta - \text{FeSi}_2$ unit cell.

Maybe discuss the std of mag and relation to energy of sqs, several cases we find large differences between SQSs. From table 9.1 we see that the stability of the relative compositions vary greatly. By introducing cobalt to the alloys, particularly at the cost of manganese result in a large positive effect on the stability, contrary replacing either manganese or nickel with titanium significantly lowers the stability. In terms of the magnetization, the results are in line with the observations of the CFMN composition, from table 9.1 it's clear that replacing either manganese or chromium drastically reduces the magnetization of the alloys. In addition, we find indication of chromium being further significant to the magnetization than manganese as seen from the first and second compounds in table 9.1

respectively. In opposition to the study of the CFMN system we observe here a clear relation between magnetization and stability. However, we are not confident if the observed outcome is a direct consequence of the magnetization or simply a product of addition of cobalt and titanium respectively to the alloys. On the other hand, in both cases the least magnetic composition is also the most unstable, thus there is weight behind the magnetic relation to stability. **Wait for CrFeMnCoSi₂ to finish**

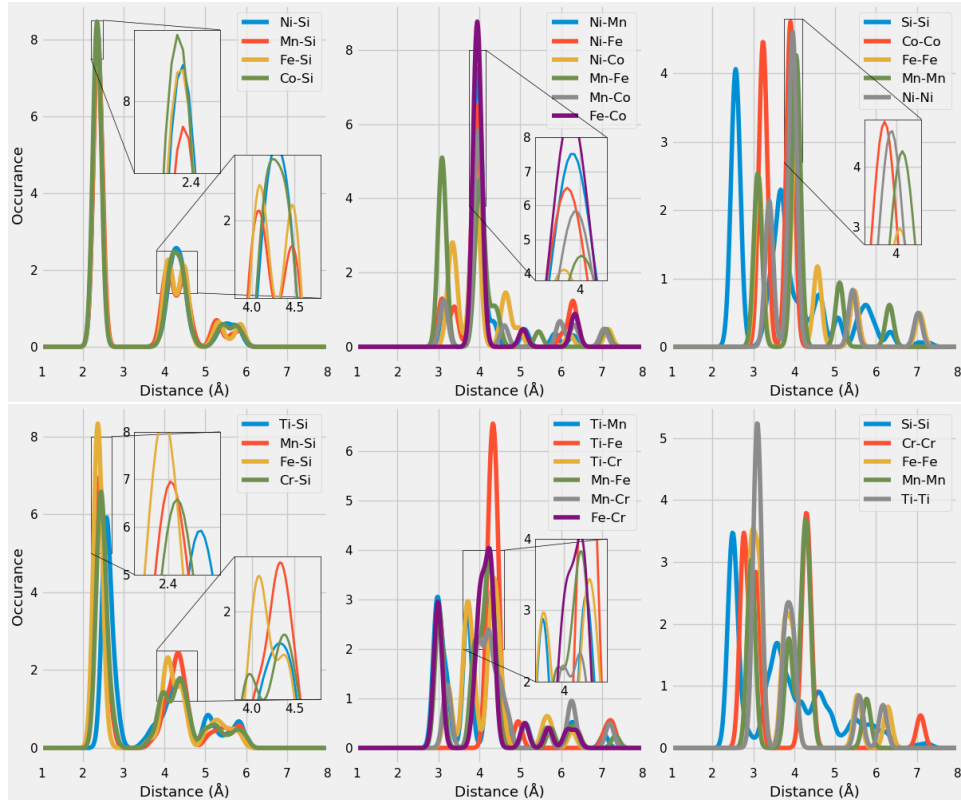


Figure 8.1: Probability distribution function of Co₄Fe₄Mn₄Ni₄Si₃₂ (top) and Cr₄Fe₄M₄Ti₄Si₃₂ (bottom)

In regards to the band gap of the compositions, we can report that a heavy majority are metals. We found no evidence of a band gap in both the CrFeCoNiSi₂ and CrFeMnTiSi₂ alloys across all supercells, as seen in the density of states of the two most stable SQSs of the respective compounds **Add figures**. Further also the most stable SQSs of the CrFeTiNiSi alloy point to a metal. Similarly the most stable SQSs of the CoFeMnNiSi₂ alloy are clearly metals. Noteworthy of this composition however is that we find clear evidence of a narrow band gap in two SQSs (A and B). In terms of stability, these lie around the mean total energy of the set. The respective band gaps are 0.033 eV in A and 0.0058 eV in B. **Include DOS or other figures for these results.**

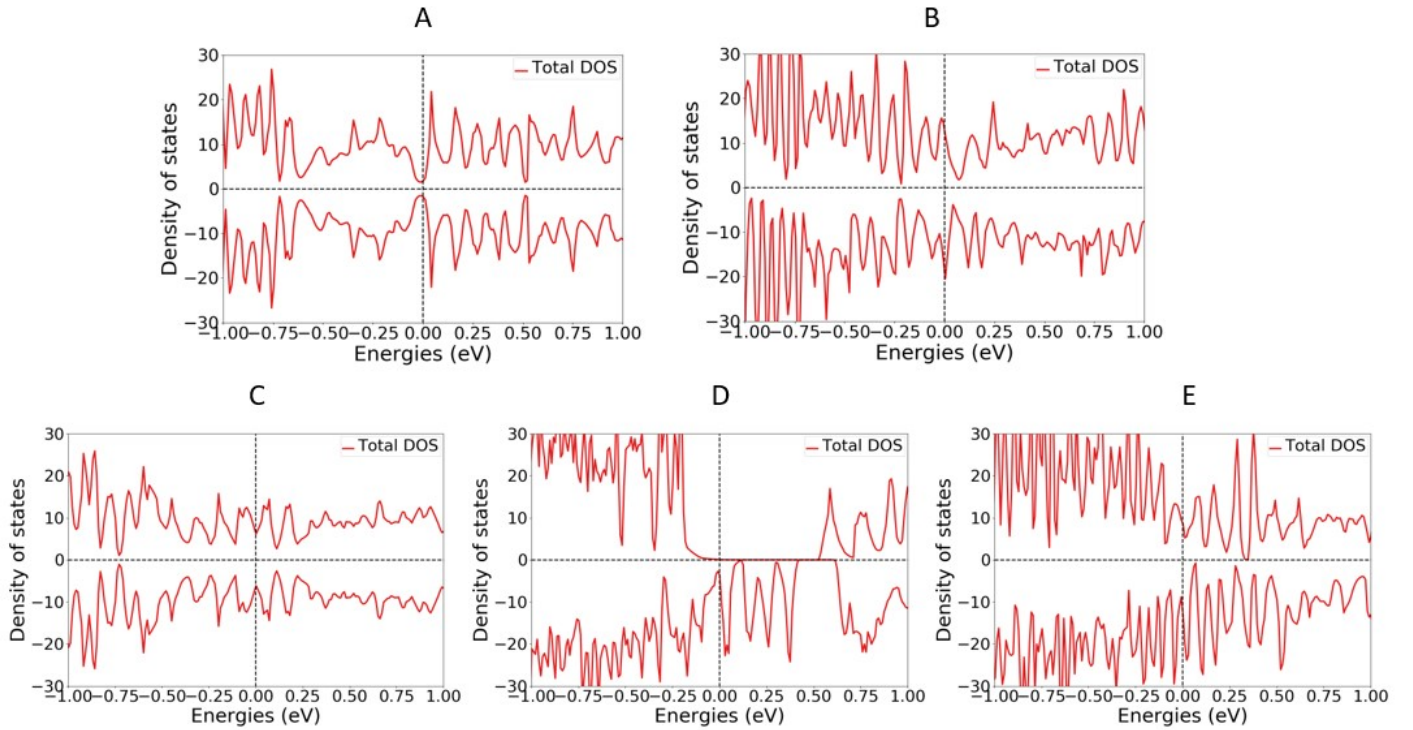


Figure 8.2: Density of states of A: CrFeCoNiSi₂, B: CrFeTiNiSi₂, C: CoFeMnNiSi₂, D: CrFeMnCoSi₂, E: CrFeMnTiSi₂. Calculations performed with PBE GGA.

To follow is details on the gaps in A and B, is it worth to include this? In the density of states plotted in figure .., the band gap in A is clearly visible. On the other hand the very narrow gap in B is not as apparent, as the states around Ef contain very small nonzero values. This could be related to the low resolution of 2500 points in the density of states as seen before, especially considering the size of the gap. In opposite to the CFMN calculations previous we here experience excellent cohesion between PBE and SCAN simulations on the band gap. With the meta-GGA functional the band gap of SQS A and B respective is 0.04 eV and the 0.003 eV. Moreover we find the identical gap transition with both functionals, which was not the case in previous endeavors with this functional. Additionally we also find that the HSE06 functional produce dissimilar results to previous experiences. In this scenario, the HSE06 functional fails to recognize the observed band gap of PBE and SCAN in both supercells. The greater number of k-points in the GGA and meta-GGA calculations offer more accurate band gaps, however lesser k-points will not result in a smaller gap, only bigger. Thus the uncertainties of previous calculations of the HSE06

functional does not apply in this case. For this reason in addition to the reputation of hybrid functionals and the lack of other factors to negatively affect the validity of the result, we find it challenging to conclude on the band gap of these structures between functionals.

Chapter 9

Overview and Outlook

The SQS size

Relevance of crystal structure

The exchange-correlation functional

What more should/could have been done in this project?

9.1 Cr₄Fe₄Mn₄Ni₄Si₃₂ in different crystal structures

In the discussion above we have covered in great detail the possibilites of high-entropy silicides based on the β - FeSi₂ unit cell with twice as many silicon atoms to 3d elements. The primary outcome and concslion of this research was that particularly the combination of Cr, Fe, Mn and Ni resulted in superiour properties in the light of the motivatian behind this project. The next question we wish to answer is if ihe promising results of the CFMN system be reproduced in other symetries. In this section we will implement the CFMN composition in crystal structures based on hexagonal CrSi₂ ($P6_{42}\bar{2}$), both tetragonal and orthorombic Mn₁₆Si₂₈ ($P\bar{4}c2$ and, Pcc a), and trigonal Fe₂Si ($P\bar{3}m1$) where we test the CFMN system to varying metal and silicon ratios, and crystal structures. As before, the total energy, enthalpy of formation and magnetic moment per atom can be found bellow in table ..

	Total energy per energy	Enthalpy of formation	Mag per atom	
CrSi2	-6.4837	0.0087	-8.1205	0.0887 0.0387
MnSi	-6.6658	0.0071	-9.1848	0.0687 0.0398
Fe2Si	-7.5082	0.0107	-10.2474	0.3848 0.0588

CrSi2

From our calculations with PBE DFT we find the bulk crsi2 material to be an indirect semiconductor with a band gap of 0.33 eV, slightly bellow the listed

value of 0.36 eV in materials project **cite**, suprinsingly we find a smaller gap of 0.32 eV from the SCAN functional. The compound is also nonmagnetic in agreement with materials project. Fore the bulk material we employed a 9 atom cell, with 6 silicon and 3 cr atoms, from this we generated SQSs of 72 atoms with the same ratio. **Include toten per atom for the unit cell? and figure of SQS + unit cell?**. For this given composistion and system we observe very similar results to that of the compositions discussed above, the eigenvalues of several SQSs report a small band gap, but its not apperant from neither the density of states or from the bandgap.py script of pymatgen. Additontly, we can not repreoduce the gap with the SCAN functional, as was possible for the CFMN (fesi2) system.

MnSi

In the tetragonal configuration, the bulk material is a nonmagnetic indirect semiconductor with a band gap of 0.76 eV accoording to our PBE calculations, and 0.78 eV from SCAN. Materials project find a band gap of 0.76 eV, in good agreement with our own PBE results. The unit cell consist of 44 total atoms, 16 manganese and 28 silicon. In the orthoromibic cell, with equal number of elements we find a band gap of 0.76 eV (0.77 ev SCAN) as well. In contrast, the CFMN alloy of both these cells produce metalic compounds. It should be noted that structures B and D in the tetragonal ssystem did not fully relax, same for D in the orthorombic cell, so these results could be inaccurate.

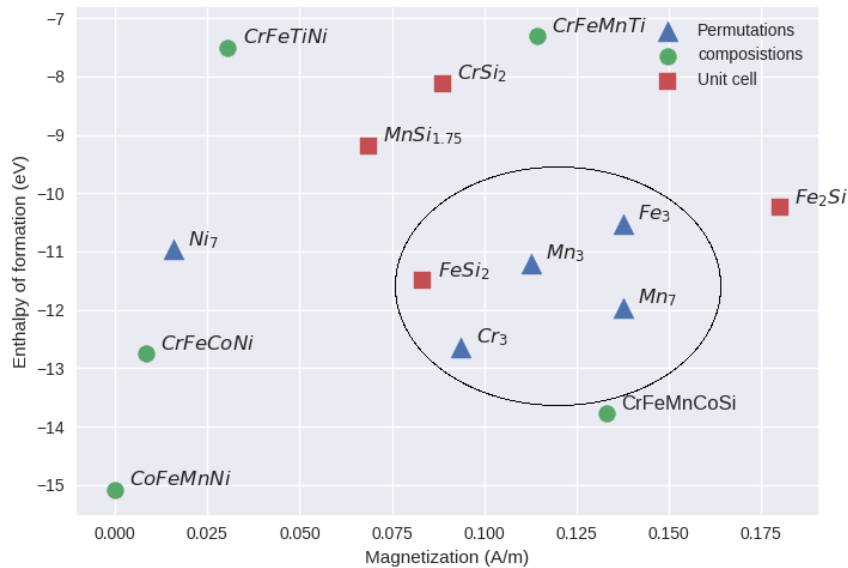
Fe2Si

In this cell, we drastically alter the metal-silicon ratio, this is seen both in the band gap and magnetic properties of the material. The magnetic moment of this cell consisting of 4 iron atoms and 2 silicon atoms is 0.67, from the iron atoms. This magnetic charachter can also be observed from the discrepancy between the two spin channels. In spin down we find a band gap of 0.21 eV, while there is no gap in spin up. This gap can also be seen in the density of states **Include figure**. This however is an abnormal result in regard to other experimental work and litterature on the Fe2Si **cite** https://www.sciencedirect.com/science/article/pii/S0925838816329796?casa_token=g9DRpu9IClcAAAAA:6Gd12A4Kh9J2igUWMVwHN8OSIKzD27VACA052FNsSAWhRY6PE. Our results are subject to errors, particularly we note that the eigenvalues used to calculate the gap contain nonphysical values in the spin down channel. However, the gap is evident in the density of states thus we include the result in this report, but acknowlendge the uncertainties revolving the value.

From this unit cell we generate 54 atom SQSs. From table .. we see that the magnetic nature remains, producing the overall highest magnetic moment of all studied supercells, which is not a surprising result considering the 3d metal to silicon ratio. **More on magnetic and total energy**. The magnetism can also be seen in the difference between the two spin channels, the bands where the occupancy transistion from 1 to 0, ie occupied to not occupied is very different. In the most magnetic supercell

D, we saw a distance of 22 bands between the spin down transition and spin up transition. Most supercells are metals from our PBE calculations. B and D show a very small gap of around 0.01 eV in one spin channel. In E we find a very narrow gap semiconductor with a total gap of 0.002 eV. This gap is surrounded by the same uncertainties as discussed previously.

9.2 Overview



Part IV

Conclusion

Write conclusion here

Appendix A

Compositions

A.1 Projected density of states

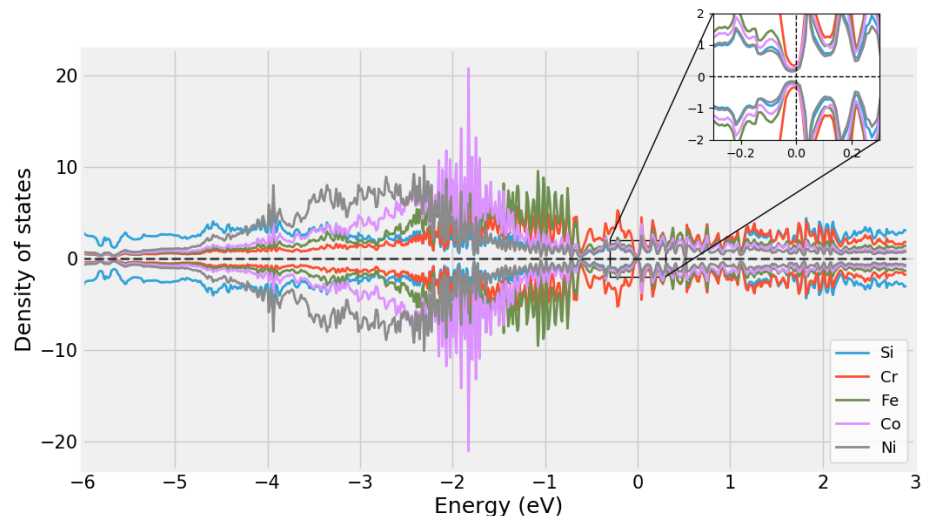


Figure A.1: chCr4Fe4Co4Ni4Si32

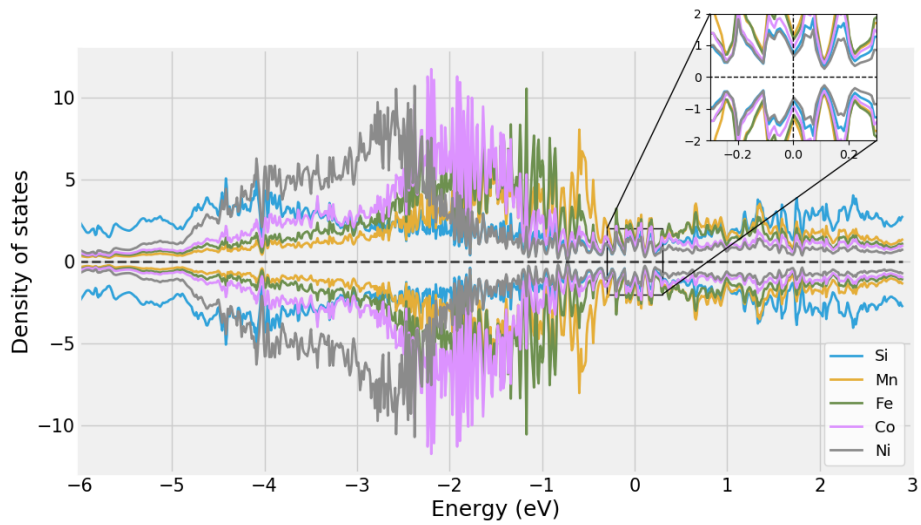


Figure A.2: chCo₄Fe₄Mn₄Ni₄Si₃₂

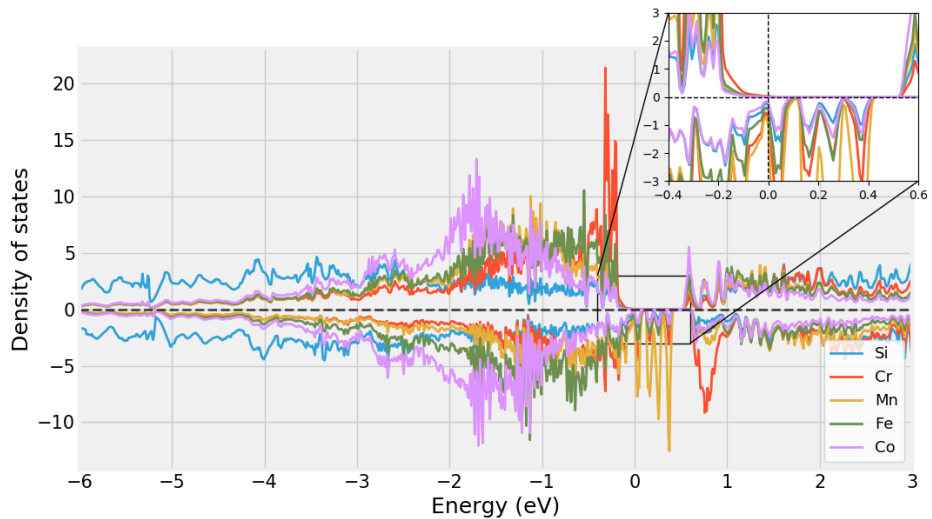


Figure A.3: chCr₄Fe₄Mn₄Co₄Si₃₂

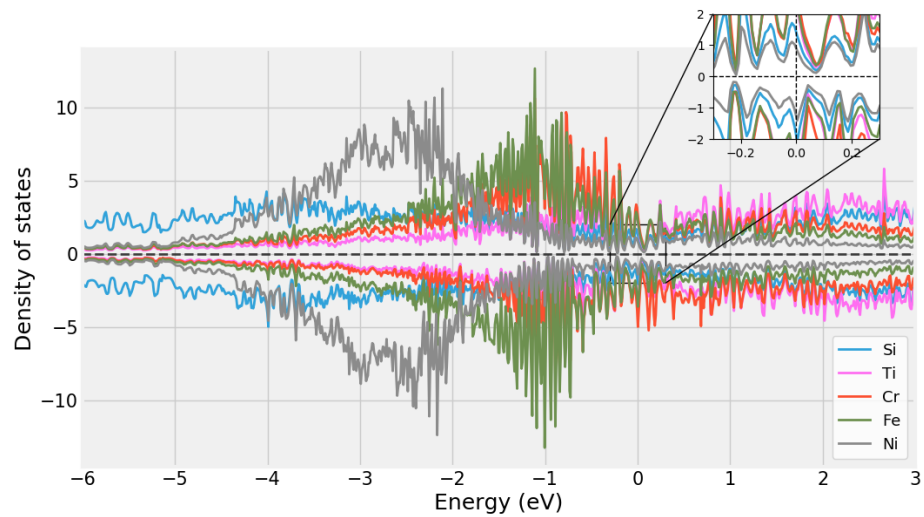


Figure A.4: chCr₄Fe₄Ti₄Ni₄Si₃₂

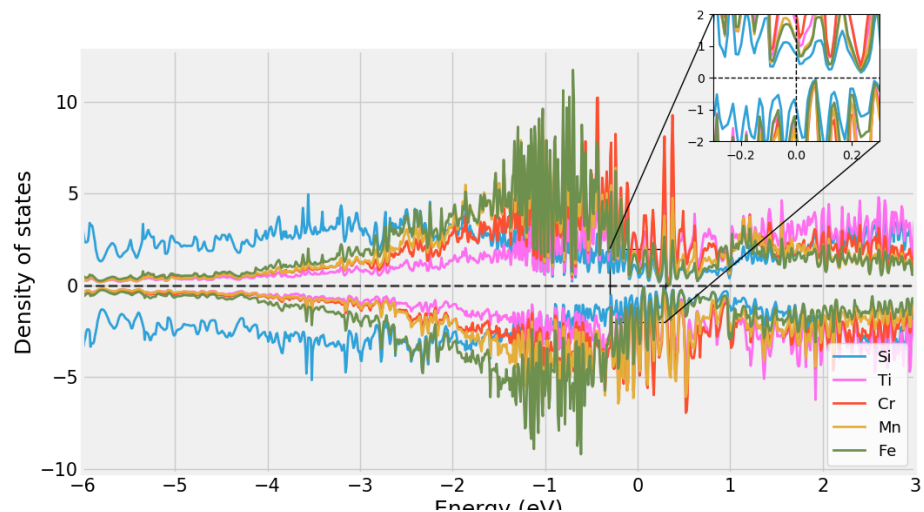


Figure A.5: chCr₄Fe₄Mn₄Ti₄Si₃₂

A.2 Probability distribution functions

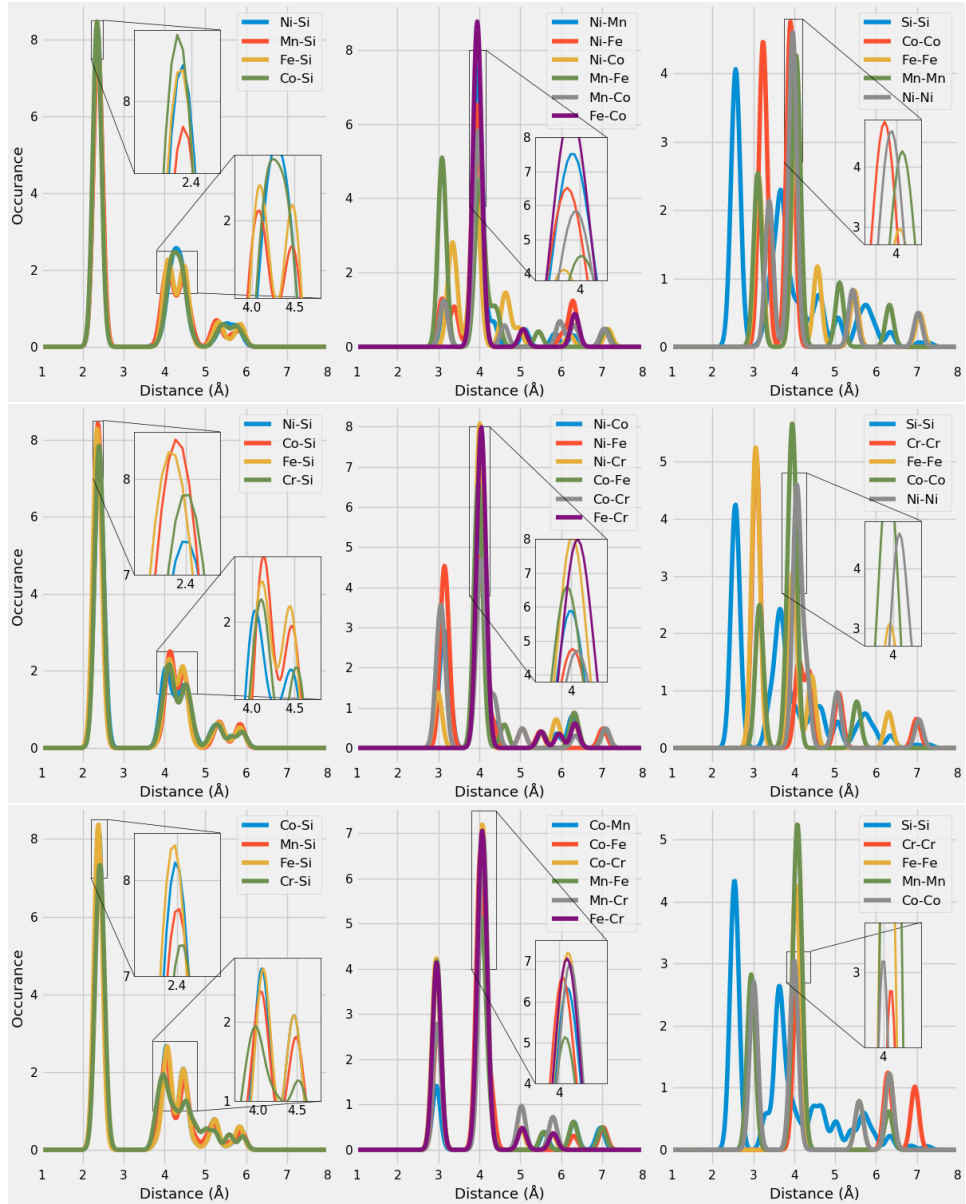


Figure A.6: Probability distribution functions of top: $\text{Co}_4\text{Fe}_4\text{Mn}_4\text{Ni}_4\text{Si}_{32}$ (SQS D), middle: $\text{Cr}_4\text{Fe}_4\text{Co}_4\text{Ni}_4\text{Si}_{32}$ (SQS B), bottom: $\text{Cr}_4\text{Fe}_4\text{Mn}_4\text{Co}_4\text{Si}_{32}$ (SQS B)

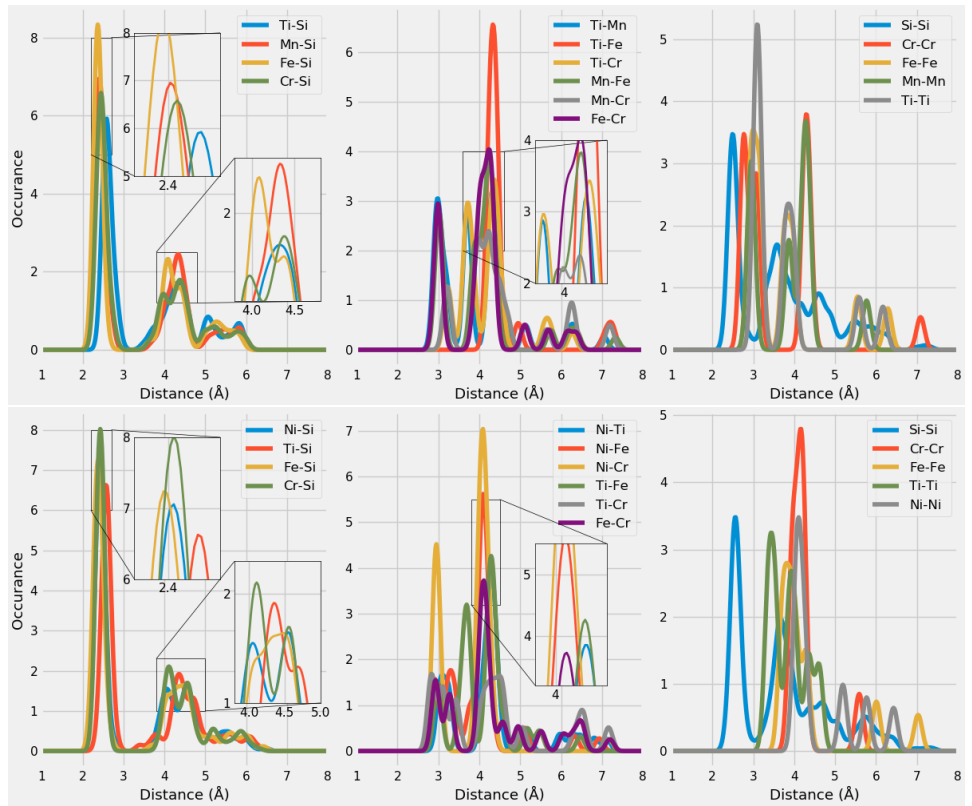


Figure A.7: Probability distribution function of top: $\text{Cr}_4\text{Fe}_4\text{Mn}_4\text{Ti}_4\text{Si}_{32}$ (SQS B), bottom: $\text{Cr}_4\text{Fe}_4\text{Ti}_4\text{Ni}_4\text{Si}_{32}$ (SQS B)

Appendix B

PDFs

something

Appendix C

Charge density

Bibliography

- [1] Jien-Wei Yeh. ‘Overview of High-Entropy Alloys’. In: *High-Entropy Alloys: Fundamentals and Applications*. Ed. by Michael C. Gao et al. Cham: Springer International Publishing, 2016, pp. 1–19. ISBN: 978-3-319-27013-5. DOI: 10.1007/978-3-319-27013-5_1. URL: https://doi.org/10.1007/978-3-319-27013-5_1.
- [2] Yong Zhang et al. ‘Phase Formation Rules’. In: *High-Entropy Alloys: Fundamentals and Applications*. Ed. by Michael C. Gao et al. Cham: Springer International Publishing, 2016, pp. 21–49. ISBN: 978-3-319-27013-5. DOI: 10.1007/978-3-319-27013-5_2. URL: https://doi.org/10.1007/978-3-319-27013-5_2.
- [3] Jien-Wei Yeh. ‘Physical Metallurgy’. In: *High-Entropy Alloys: Fundamentals and Applications*. Ed. by Michael C. Gao et al. Cham: Springer International Publishing, 2016, pp. 51–113. ISBN: 978-3-319-27013-5. DOI: 10.1007/978-3-319-27013-5_3. URL: https://doi.org/10.1007/978-3-319-27013-5_3.
- [4] Jien-Wei Yeh et al. ‘Functional Properties’. In: *High-Entropy Alloys: Fundamentals and Applications*. Ed. by Michael C. Gao et al. Cham: Springer International Publishing, 2016, pp. 237–265. ISBN: 978-3-319-27013-5. DOI: 10.1007/978-3-319-27013-5_7. URL: https://doi.org/10.1007/978-3-319-27013-5_7.
- [5] Lewis Robert Owen and Nicholas Gwilym Jones. ‘Lattice distortions in high-entropy alloys’. In: *Journal of Materials Research* 33.19 (2018), pp. 2954–2969. DOI: 10.1557/jmr.2018.322.
- [6] Fuyang Tian. ‘A Review of Solid-Solution Models of High-Entropy Alloys Based on Ab Initio Calculations’. In: *Frontiers in Materials* 4 (2017). ISSN: 2296-8016. DOI: 10.3389/fmats.2017.00036. URL: <https://www.frontiersin.org/article/10.3389/fmats.2017.00036>.
- [7] S.-H. Wei et al. ‘Electronic properties of random alloys: Special quasirandom structures’. In: *Phys. Rev. B* 42 (15 Nov. 1990), pp. 9622–9649. DOI: 10.1103/PhysRevB.42.9622. URL: <https://link.aps.org/doi/10.1103/PhysRevB.42.9622>.
- [8] Z. W. Lu, S.-H. Wei and Alex Zunger. ‘Electronic structure of ordered and disordered Cu₃ Au and Cu₃ Pd’. In: *Phys. Rev. B* 45 (18 May 1992), pp. 10314–10330. DOI: 10.1103/PhysRevB.45.10314. URL: <https://link.aps.org/doi/10.1103/PhysRevB.45.10314>.

- [9] Su-Huai Wei and Alex Zunger. ‘Band offsets and optical bowings of chalcopyrites and Zn-based II-VI alloys’. In: *Journal of Applied Physics* 78.6 (1995), pp. 3846–3856. DOI: 10.1063/1.359901. eprint: <https://doi.org/10.1063/1.359901>. URL: <https://doi.org/10.1063/1.359901>.
- [10] Michael C. Gao et al. ‘Applications of Special Quasi-random Structures to High-Entropy Alloys’. In: *High-Entropy Alloys: Fundamentals and Applications*. Ed. by Michael C. Gao et al. Cham: Springer International Publishing, 2016, pp. 333–368. ISBN: 978-3-319-27013-5. DOI: 10.1007/978-3-319-27013-5_10. URL: https://doi.org/10.1007/978-3-319-27013-5_10.
- [11] A. van de Walle et al. ‘Efficient stochastic generation of special quasirandom structures’. In: *Calphad* 42 (2013), pp. 13–18. ISSN: 0364-5916. DOI: <https://doi.org/10.1016/j.calphad.2013.06.006>. URL: <https://www.sciencedirect.com/science/article/pii/S0364591613000540>.
- [12] Shen Wang et al. ‘Comparison of two calculation models for high entropy alloys: Virtual crystal approximation and special quasi-random structure’. In: *Materials Letters* 282 (2021), p. 128754. ISSN: 0167-577X. DOI: <https://doi.org/10.1016/j.matlet.2020.128754>. URL: <https://www.sciencedirect.com/science/article/pii/S0167577X20314610>.
- [13] Peng Wei et al. ‘Understanding magnetic behaviors of FeCoN-iSi0.2M0.2 (M=Cr, Mn) high entropy alloys via first-principle calculation’. In: *Journal of Magnetism and Magnetic Materials* 519 (2021), p. 167432. ISSN: 0304-8853. DOI: <https://doi.org/10.1016/j.jmmm.2020.167432>. URL: <https://www.sciencedirect.com/science/article/pii/S0304885320323994>.
- [14] Muhammad Rashid et al. ‘Ab-initio study of fundamental properties of ternary ZnO_{1-x}S_x alloys by using special quasi-random structures’. In: *Computational Materials Science* 91 (2014), pp. 285–291. ISSN: 0927-0256. DOI: <https://doi.org/10.1016/j.commatsci.2014.04.032>. URL: <https://www.sciencedirect.com/science/article/pii/S0927025614002742>.
- [15] V. Sorkin et al. ‘First-principles-based high-throughput computation for high entropy alloys with short range order’. In: *Journal of Alloys and Compounds* 882 (2021), p. 160776. ISSN: 0925-8388. DOI: <https://doi.org/10.1016/j.jallcom.2021.160776>. URL: <https://www.sciencedirect.com/science/article/pii/S092583882102185X>.
- [16] Daniel W. Hook, Simon J. Porter and Christian Herzog. ‘Dimensions: Building Context for Search and Evaluation’. In: *Frontiers in Research Metrics and Analytics* 3 (2018). <https://www.frontiersin.org/articles/10.3389/frma.2018.00023/pdf>, p. 23. DOI: 10.3389/frma.2018.00023. URL: <https://app.dimensions.ai/details/publication/pub.1106289502>.
- [17] Clas Persson. *A Brief Introduction to the Density Functional Theory*. 1st ed. Department of Physics, University of Oslo, 2020.
- [18] David S. Sholl and Janice A. Steckel. ‘Density functional theory a practical introduction’. In: (2009).

- [19] David J Griffiths. *Introduction to Quantum Mechanics*. 2nd ed. Cambridge University Press, 2016, p. 465. ISBN: 9781107179868.
- [20] Aron J. Cohen, Paula Mori-Sánchez and Weitao Yang. ‘Insights into Current Limitations of Density Functional Theory’. In: *Science* 321.5890 (2008), pp. 792–794. DOI: 10.1126/science.1158722. eprint: <https://www.science.org/doi/pdf/10.1126/science.1158722>. URL: <https://www.science.org/doi/abs/10.1126/science.1158722>.
- [21] John P. Perdew and Mel Levy. ‘Physical Content of the Exact Kohn-Sham Orbital Energies: Band Gaps and Derivative Discontinuities’. In: *Phys. Rev. Lett.* 51 (20 Nov. 1983), pp. 1884–1887. DOI: 10.1103/PhysRevLett.51.1884. URL: <https://link.aps.org/doi/10.1103/PhysRevLett.51.1884>.
- [22] Michael Foster and Karl Sohlberg. ‘Empirically corrected DFT and semi-empirical methods for non-bonding interactions’. In: *Physical Chemistry Chemical Physics - PHYS CHEM CHEM PHYS* 12 (Jan. 2010). DOI: 10.1039/b912859j.
- [23] Carlos Borca (<https://scicomp.stackexchange.com/users/8020/carlos-borca>). *Limitations of Density Functional Theory as a computational method?* Computational Science Stack Exchange. eprint: <https://scicomp.stackexchange.com/q/11443>. URL: <https://scicomp.stackexchange.com/q/11443>.
- [24] NobelPrize.org. *The Nobel Prize in Chemistry 1998*. Accessed: 2022-15-04. URL: <https://www.nobelprize.org/prizes/chemistry/1998/summary/>.
- [25] John P Perdew and Yue Wang. ‘Accurate and simple analytic representation of the electron-gas correlation energy’. In: *Physical review B* 45.23 (1992), p. 13244.
- [26] John P Perdew, Kieron Burke and Matthias Ernzerhof. ‘Generalized gradient approximation made simple’. In: *Physical review letters* 77.18 (1996), p. 3865.
- [27] Fabian (<https://mattermodeling.stackexchange.com/users/295/fabian>). *What makes PBE the most preferred functional over other GGA functionals?* Matter Modeling Stack Exchange. URL: <https://mattermodeling.stackexchange.com/q/402>.
- [28] Jianmin Tao et al. ‘Climbing the Density Functional Ladder: Nonempirical Meta-Generalized Gradient Approximation Designed for Molecules and Solids’. In: *Phys. Rev. Lett.* 91 (14 Sept. 2003), p. 146401. DOI: 10.1103/PhysRevLett.91.146401. URL: <https://link.aps.org/doi/10.1103/PhysRevLett.91.146401>.
- [29] Fabien Tran and Peter Blaha. ‘Importance of the Kinetic Energy Density for Band Gap Calculations in Solids with Density Functional Theory’. In: *The Journal of Physical Chemistry A* 121.17 (2017). PMID: 28402113, pp. 3318–3325. DOI: 10.1021/acs.jpca.7b02882. eprint: <https://doi.org/10.1021/acs.jpca.7b02882>. URL: <https://doi.org/10.1021/acs.jpca.7b02882>.

- [30] Jianwei Sun, Adrienn Ruzsinszky and John P. Perdew. ‘Strongly Constrained and Appropriately Normed Semilocal Density Functional’. In: *Phys. Rev. Lett.* 115 (3 July 2015), p. 036402. DOI: 10.1103/PhysRevLett.115.036402. URL: <https://link.aps.org/doi/10.1103/PhysRevLett.115.036402>.
- [31] Arup Chakraborty et al. ‘Predicting accurate cathode properties of layered oxide materials using the SCAN meta-GGA density functional’. In: *npj Computational Materials* 4.1 (2018), pp. 1–9.
- [32] Tomáš Rauch et al. ‘Defect levels from SCAN and MBJ meta-GGA exchange-correlation potentials’. In: *Phys. Rev. B* 104 (6 Aug. 2021), p. 064105. DOI: 10.1103/PhysRevB.104.064105. URL: <https://link.aps.org/doi/10.1103/PhysRevB.104.064105>.
- [33] Jianwei Sun et al. ‘Accurate first-principles structures and energies of diversely bonded systems from an efficient density functional’. In: *Nature chemistry* 8.9 (2016), pp. 831–836.
- [34] Eric B. Isaacs and Chris Wolverton. ‘Performance of the strongly constrained and appropriately normed density functional for solid-state materials’. In: *Phys. Rev. Materials* 2 (6 June 2018), p. 063801. DOI: 10.1103/PhysRevMaterials.2.063801. URL: <https://link.aps.org/doi/10.1103/PhysRevMaterials.2.063801>.
- [35] Axel D Becke and Erin R Johnson. ‘A simple effective potential for exchange’. In: *The Journal of chemical physics* 124.22 (2006), p. 221101.
- [36] Pedro Borlido et al. ‘Large-Scale Benchmark of Exchange–Correlation Functionals for the Determination of Electronic Band Gaps of Solids’. In: *Journal of Chemical Theory and Computation* 15.9 (2019). PMID: 31306006, pp. 5069–5079. DOI: 10.1021/acs.jctc.9b00322. eprint: <https://doi.org/10.1021/acs.jctc.9b00322>. URL: <https://doi.org/10.1021/acs.jctc.9b00322>.
- [37] Carlo Adamo and Vincenzo Barone. ‘Toward reliable density functional methods without adjustable parameters: The PBE0 model’. In: *The Journal of Chemical Physics* 110.13 (1999), pp. 6158–6170. DOI: 10.1063/1.478522. eprint: <https://doi.org/10.1063/1.478522>. URL: <https://doi.org/10.1063/1.478522>.
- [38] Aliaksandr V. Krukau et al. ‘Influence of the exchange screening parameter on the performance of screened hybrid functionals’. In: *The Journal of Chemical Physics* 125.22 (2006), p. 224106. DOI: 10.1063/1.2404663. eprint: <https://doi.org/10.1063/1.2404663>. URL: <https://doi.org/10.1063/1.2404663>.
- [39] Jochen Heyd, Gustavo E Scuseria and Matthias Ernzerhof. ‘Hybrid functionals based on a screened Coulomb potential’. In: *The Journal of chemical physics* 118.18 (2003), pp. 8207–8215.
- [40] Paula Mori-Sánchez and Aron J. Cohen. ‘The derivative discontinuity of the exchange–correlation functional’. In: *Phys. Chem. Chem. Phys.* 16 (28 2014), pp. 14378–14387. DOI: 10.1039/C4CP01170H. URL: <http://dx.doi.org/10.1039/C4CP01170H>.

- [41] G. Kresse and D. Joubert. ‘From ultrasoft pseudopotentials to the projector augmented-wave method’. In: *Phys. Rev. B* 59 (3 Jan. 1999), pp. 1758–1775. DOI: 10.1103/PhysRevB.59.1758. URL: <https://link.aps.org/doi/10.1103/PhysRevB.59.1758>.
- [42] P. E. Blöchl. ‘Projector augmented-wave method’. In: *Phys. Rev. B* 50 (24 Dec. 1994), pp. 17953–17979. DOI: 10.1103/PhysRevB.50.17953. URL: <https://link.aps.org/doi/10.1103/PhysRevB.50.17953>.
- [43] Peter E. Blöchl, O. Jepsen and O. K. Andersen. ‘Improved tetrahedron method for Brillouin-zone integrations’. In: *Phys. Rev. B* 49 (23 June 1994), pp. 16223–16233. DOI: 10.1103/PhysRevB.49.16223. URL: <https://link.aps.org/doi/10.1103/PhysRevB.49.16223>.
- [44] Jürgen Furthmüller. *How might I calculate the exact bandgap from DOSCAR ?* May 2015.